CHEMICAL REVIEWS

Review

pubs.acs.org/CR

Graphene Materials and Their Use in Dye-Sensitized Solar Cells

Joseph D. Roy-Mayhew[†,‡] and Ilhan A. Aksay[†,*]

[†]Department of Chemical & Biological Engineering, Princeton University, Princeton, New Jersey 08544, United States

[‡]Vorbeck Materials Corporation, 8306 Patuxent Range Road Suite 103, Jessup, Maryland 20794, United States

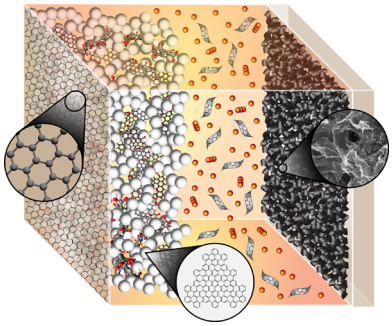

CONTENTS

1. INTRODUCTION

Dye-sensitized solar cells (DSSCs) have taken up broad interest as a promising low-cost solar cell technology since they were first reported on in 1991.[1] DSSCs use specialized materials for specific cell functions such as photon absorption, charge separation, and charge transport. Figure 1 depicts a simple energy diagram of how these devices function. A photon enters the solar cell through a transparent electrode and can be absorbed by a sensitizer, exciting an electron (a), as shown in Figure 1A. Then this electron can be injected into the conduction band of a neighboring semiconductor (b) and diffuse to the current collector (c). The electron can perform work and flow to the cathode (d) where it is transferred to an electrolyte or a hole conductor (e). This material can then transfer an electron to the sensitizer (f), regenerating it and completing the circuit. To optimize these devices and achieve respectable power conversion efficiencies (η, defined as the ratio of power incident on the solar cell to the maximum power produced by the solar cell; see Box 1 for details on solar cell characterization) researchers have looked at ways to (i) maximize light harvesting and (ii) minimize losses due to parasitic electron transfer pathways (v, w, x, y, and z in Figure 1B) while also minimizing the overpotentials required to drive the electron transfer in the desired direction (colored bands in Figure 1B).

Toward these ends, the archetypical DSSC (Figure 2) uses a fluorine-doped tin oxide (FTO) transparent electrode with a sintered titania (anatase phase) nanoparticle scaffold sensitized with organometallic dye molecules as the photoanode, an iodide/triiodide redox couple dissolved in acetonitrile as the electrolyte, and a platinized FTO cathode. These components have led to favorable device kinetics as outlined in Table 1.

TiO_2 nanoparticles provide a high surface area film (~1000× roughness for 10 μm thick) for increased dye loading, while sintering ensures high connectivity of the particles for fast electron transport and mechanical stability. DSSC dyes absorb light strongly in the visible range, they have extended excited state lifetimes, and their binding to the titania scaffold improves stability and charge transport.[3] For instance, a ruthenium bipyridyl dye, N719, absorbs light with wavelengths up to ~800 nm, has an extinction coefficient of ~1.5×10^4 $M^{-1}\cdot cm^{-1}$ (at 535 nm),[4] and has carboxylic acid groups that facilitate chemisorption to the titania scaffold.[3] In the electrolyte, acetonitrile has been the solvent of choice for high-efficiency cells due to its low viscosity (0.34 mPa·s at 25 °C), facilitating ion transport, and its high electrochemical stability.[3] However, the low boiling point and thus high volatility of the solvent inhibits the long-term stability of devices. To improve device stability, higher viscosity solvents are commonly mixed with acetonitrile (i.e., valeronitrile) or used on their own (i.e., methoxypropionitrile). The iodide/triiodide redox mediator was used in the original DSSC and had an unmatched efficiency until 2012, when a record DSSC (η = 12.3%) using a cobalt-based mediator was reported. In a simplistic view of this system, iodide regenerates the dye forming triiodide. Triiodide then diffuses to the cathode and is reduced back to iodide, which in turn can diffuse back to the photoanode and continue the cycle.

A primary reason for the success of the iodide/triiodide mediator is that electron transfer from the photoanode to triiodide is slow (recombination pathway x in Figure 1B), reducing recombination in the solar cell. Nevertheless, at the cathode, triiodide must be reduced quickly (i.e., with a

Received: July 30, 2013

   dx.doi.org/10.1021/cr400412a | Chem. Rev. XXXX, XXX, XXX–XXX

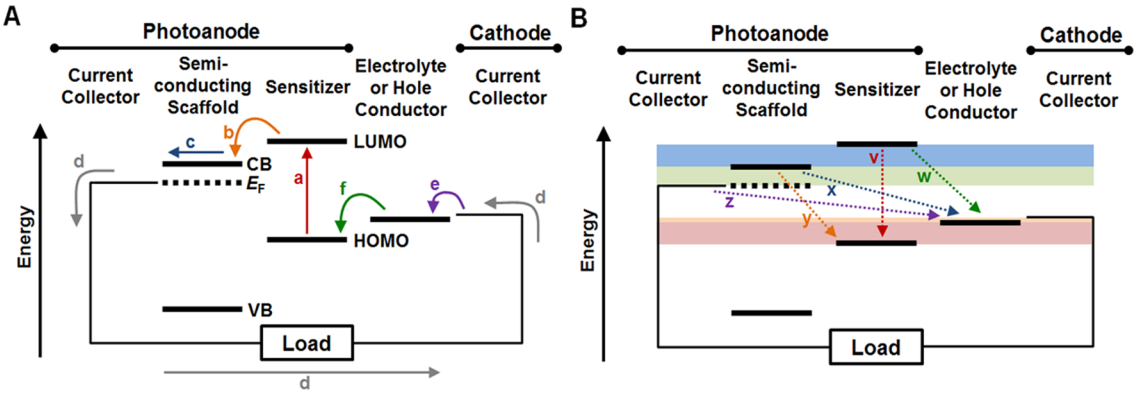

Figure 1. Energy diagram for a DSSC. CB and VB refer to the conduction band and valence band, respectively. E_F represents the Fermi level of the semiconductor and is represented near CB due to a high level of electronic doping. LUMO and HOMO levels are the least unoccupied and highest unoccupied molecular orbitals of the sensitizer. For traditional DSSC architectures, at least one current collector must be a transparent electrode to allow light into the cell. (A) Desired electron pathway. Colored arrows a, b, c, d, e, and f represent some of the energy transfer steps as described in the main text. (B) Major recombination pathways. Colored arrows v, w, x, y, and z represent some parasitic recombination pathways. Voltage drops for different charge transfer steps are represented by the colored bands. Adapted with permission from ref 2. Copyright 2013 Joseph Roy-Mayhew.

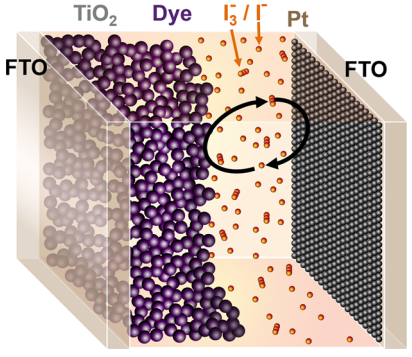

Figure 2. Schematic of a typical DSSC. The primary particle diameter of TiO_2 used is 10−20 nm, and the phase is anatase. Void space is about 50%. FTO generally has a sheet resistance of ∼15 Ω/sq and transmittance in the visible of ∼85%. Platinum nanoparticles typically are created through thermolysis of chloroplatinic acid. Reprinted with permission from ref 2. Copyright 2013 Joseph Roy-Mayhew.

Table 1. DSSC Kinetics Values as Reported by Hagfeldt et al.[3]

desired pathway	time constant (s)	recombination pathway	time constant (s)
b	10^{-1}–10^{-3}	v	10^{-8}
d	10^{-2}–10^{-4}	x	10^{-2}
f	10^{-6}–10^{-10}	y	10^{-4}

minimum overpotential), dictating the necessity of a catalyst. Cathodes composed of platinum nanoparticles deposited on FTO have been widely used due to their facile fabrication, high activity for the iodide/triiodide mediator, and sufficient corrosion resistance to iodo species present in the electrolyte.[5−8] Detailed descriptions of each component as well as recent advances can be found in a recent book edited by Kalyanasundaram[9] and several recent reviews.[3,10,11]

To advance performance and lower cost, incorporation of new materials and processing techniques is actively pursued. For instance, organic dyes, which avoid the use of rare earth metals, have been developed which have extinction coefficients an order of magnitude greater than the traditional ruthenium complexes.[11,12] Additionally, both solid-state hole conductors and ionic liquids which have negligible vapor pressure and high ionic conductivities have been explored to replace the traditional organic electrolytes.[13−16] At the cathode, transition metal compounds,[17,18] conducting polymers,[19] and carbon materials[20−25] have been introduced as alternative catalysts to platinum.

Graphene materials, with their exceptional electrical, optical, and mechanical properties, have been incorporated into each aspect of a DSSC (see Figure 3). They were first used in 2008

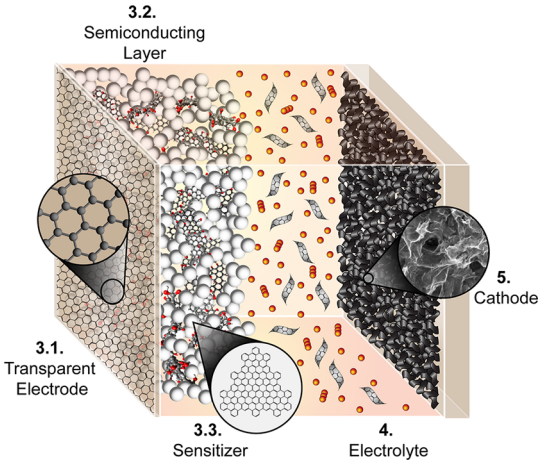

Figure 3. Schematic of a DSSC incorporating graphene materials in each part of the device. Numbers represent the section in which particular studies are discussed in this review. For instance, use of graphene materials as a transparent electrode for DSSCs is discussed in section 3.1. Adapted with permission from ref 2. Copyright 2013 Joseph Roy-Mayhew.

as a transparent electrode to replace FTO at the photoanode[26] and have since been used, for example, with the purpose of harvesting light,[27] improving transport through both the titania layer[28−34] and the electrolyte,[35,36] and superseding platinum at the cathode,[37−39] as will be discussed in this review.

Due to their multifunctionality, it is no surprise that graphene materials have quickly made their entry into DSSC applications. A simple ISI Web of Knowledge search shows the rapid increase in the number of publications on graphene, DSSCs, and graphene in DSSCs (see Figure 4). With thousands

dx.doi.org/10.1021/cr400412a | Chem. Rev. XXXX, XXX, XXX−XXX

Box 1

A standard technique to measure solar cell performance is a current−voltage ($I-V$) or current density−voltage ($J-V$) curve. By performing a voltage sweep with a device that can uptake load, such as a potentiostat, or by running a current through a solar cell at variable external resistances one can generate a $J-V$ curve. When applying light with a well-defined spectrum and intensity (e.g., AM1.5G solar simulation) to a solar cell and then measuring its $J-V$ response, several solar cell parameters can be deduced as demonstrated in the figure below. These parameters are often used to compare results arising from various laboratories. The open circuit voltage (V_{OC}) is the potential difference of the cell when no current is drawn (e.g., when $I = 0$, resistance $\rightarrow \infty$). The short circuit current (I_{SC}) is the current produced through the cell when no external load is applied (e.g., when $V = 0$, resistance $\rightarrow 0$). In general, a solar cell's V_{OC} is bounded by the band gap of the absorbing material, and the I_{SC} is bounded by the number of photons incident on the solar cell with energy greater than the band gap. A device's fill factor (FF) is the ratio of the maximum power (P_{Max}) that can be obtained from the solar cell to the product of V_{OC} and I_{SC} (i.e., the ratio of the area bounded by the gray dotted line to the area bounded by the blue dotted line in the figure below). Higher resistance and more recombination in a solar cell reduce the device's FF. The power conversion efficiency, η, of a solar cell is defined as the ratio of P_{Max} to the power incident on the solar cell (P_{In}) per area. Often current density (J) is reported rather than current as the former normalizes the value with respect to electrode area. To prevent stray light from influencing the measurements and control the active area for testing, an opaque mask with a predefined window area is often used. The relations describing common solar cell parameters are summarized by the following equation:

$$\eta = \frac{P_{Max}}{P_{In}} = \frac{FF \cdot J_{SC} V_{OC}}{P_{In}}$$

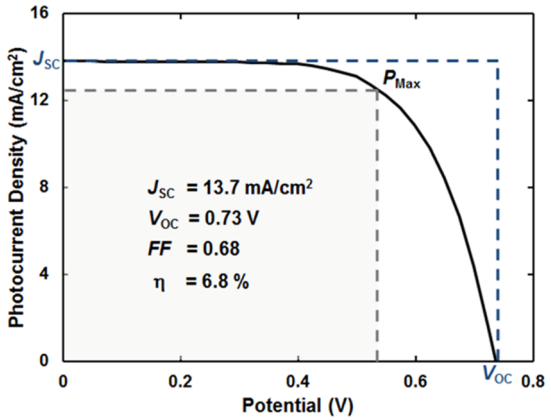

Above: A sample DSSC J-V curve obtained under 1,000 W/m² AM1.5G solar simulation. The J_{SC}, V_{OC}, and P_{Max} points are highlighted, and solar cell characteristics tabulated under the curve. The FF can be determine as the ratio of the area enclosed by the gray dotted tines, to the area enclosed by the blue dotted lines. Reprinted with permission from ref 2. Copyright 2013 Joseph Roy-Mayhew.

of papers on graphene and dye-sensitized solar cells published each year and over 100 papers published in 2012 combining the topics, the area is ripe for a review.

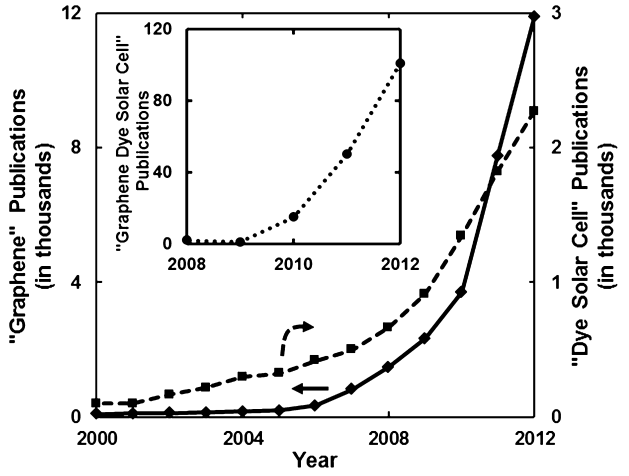

Figure 4. Number of yearly publications with keywords of "graphene" or "dye solar cell" since 2000. (Inset) Yearly publications for "graphene" and "dye solar cell".

Herein, we provide a comprehensive review of the use of graphene materials in DSSCs up through 2012, inclusive, and critically evaluate the goals of using the material in each aspect of a DSSC, highlighting the major discrepancies which need further research for clarification. We also describe how the various production methods of graphene materials lead to materials with different properties and focus on how these properties affect device properties. By doing so, we aim to build upon the literature to suggest ways to not only to engineer better devices but also to define research goals for further developments. We begin by introducing graphene and the fabrication methods to produce the material as well as other related graphene-like materials. Then, we discuss the properties of these materials and their use in each area of a DSSC.

2. GRAPHENE MATERIALS

The term graphene has been used loosely in the literature to represent pristine graphene as well as many other materials with some similar characteristics, all of which we include under the umbrella of graphene materials. Depending on how they are produced, these materials can have vastly different chemical structures and thus properties. Ideally, we should be able to identify each material by its exact chemical makeup or at least by its properties. However, currently there are no standard criteria to evaluate graphene materials with, and information provided by authors is understandably incomplete. Thus, in this review we seek to give readers a sense of what the structure and properties of the graphene materials used are by providing basic information on the fabrication technique, with the idea that materials produced in similar ways will have similar structural features and properties. A comprehensive description of graphene materials' production techniques and properties is not provided as they can be found in various recent publications.[40−53]

Pristine graphene, as the basal plane of graphite, is an atomic layer of sp^2-hybridized carbon arranged with a honeycomb structure. Many of the advantages of the material come from quantum effects prominent when it is present in its single atomic layer, and to lesser extent few layer, form. Preventing aggregation and restacking to a graphitic structure is a main challenge of working with the material due to attractive van der Waals interactions. Staggered stacks of graphene, which have an

dx.doi.org/10.1021/cr400412a | Chem. Rev. XXXX, XXX, XXX−XXX

interlayer spacing of 0.34 nm, make up graphite.[54] Studies which aim to use pristine graphene are currently limited to low-throughput production techniques such as mechanical exfoliation ("Scotch Tape" method),[55,56] liquid exfoliation,[57,58] epitaxial growth,[49,59−61] and chemical vapor deposition (CVD).[47,49,62,63] These methods result in monolayers of the material on a substrate (~0.8 mg/m^2) or very dilute suspensions (~0.01 mg/mL).[57]

Both liquid-exfoliated graphene and CVD-derived graphene have been used in DSSC applications. Liquid exfoliation involves sonication of graphite in the presence of a solvent (e.g., *N*-methyl-pyrrolidone) which has a surface energy close to that of graphite (ideally it would match) with the idea that the interfacial energy between the solvent and graphene would be minimized as would the van der Waals forces between graphene sheets.[57,58] The resulting suspension is a mixture of single, few, and multilayered graphene sheets. The concentration of graphene can be increased by additional sonication and recycling of the sediments. For CVD, a gaseous carbonaceous precursor (e.g., methane) is flowed at high temperatures (~1000 °C) over a metal substrate. The most common metals used are copper and nickel. They were chosen in part due to their catalytic activity toward hydrocarbon decomposition and in part due to the low solubility of carbon in them, both of which are important to facilitate production of atomically thin films.[47] As detailed in the reviews, much research is ongoing to reduce the number of defects and grains in CVD-derived graphene and improve the concentration of single-sheet liquid-exfoliated graphene so that the materials behave more like pristine graphene.

We report briefly on the properties of pristine graphene, but much more information can be found in the aforementioned reviews. The intrinsic room-temperature electron mobility for pristine graphene has been reported to be as high as 200 000 cm^2/(V·s),[64,65] but most reported values fall between 3000 and 15 000 cm^2/(V·s).[43] This value is highly influenced by the substrate and whether any grain boundaries are present.[62] Although mobility is high, due to the low intrinsic charge carrier concentration, the sheet resistance (R_{Sh}) of a single layer of graphene is ~6.45 kΩ/sq.[66] Electronic doping can reduce the resistance by over an order of magnitude.[65,67] Pristine graphene has been shown to exhibit strength and modulus of 130 GPa and 1.0 TPa, respectively.[68] The material also has very high optical absorption properties (~2.3% of light is captured per sheet[69]); however, due to the other exceptional properties, its absorption per unit modulus or per unit electron mobility is low, presenting it as a strong candidate for transparent applications. Furthermore, being only an atom thick, the material has a specific surface area calculated to be 2630 m^2/g.[70,71]

To date, reducing graphene oxide has been the most promising approach for bulk production of graphene materials. In this approach, graphite is first oxidized using strong oxidants and intercalating compounds by methods that date back to 1840 (e.g., H_2SO_4, HNO_3, $KMnO_4$, $KClO_3$, $NaClO_2$).[72−77] In experimental studies, fully oxidized graphite has primarily been reported with a molar carbon to oxygen ratio (C/O) of ~2 and is called graphite oxide.[78,79] At least one study reports C/O values as low as 1.3,[80] and theoretical modeling studies suggest materials with this composition are stable;[81] however, experimental observation is complicated by the existence of adsorbed water. Graphite oxide can be exfoliated in water through ultrasonic agitation producing stable suspensions of graphene oxide as first demonstrated by Tanaka.[82,83] We note that the acronym GO is commonly used for both graphite oxide and graphene oxide, and some studies do not distinguish between the two materials, even though they have different properties much like graphene and graphite do. To avoid confusion on the source, we will avoid the usage of the GO acronym alone either for graphite oxide or graphene oxide. Detailed reviews of the properties and proposed structure of graphene oxide can be found in the literature, though we note that specific oxygen groups and their locations on the lattice will vary by oxidation method.[79,84] A recent model structure derived from spectroscopic analysis by Gao et al.[85] is presented in Figure 5.

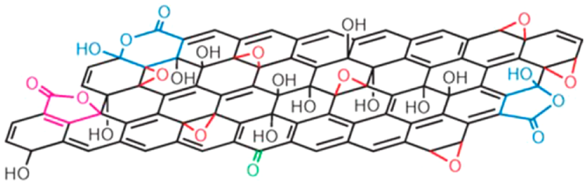

Figure 5. Proposed structure of graphene oxide. Reprinted with permission from Macmillan Publishers Ltd. *Nature Chemistry* from ref 85, copyright 2009.

Graphene oxide can be reduced by chemical, electrochemical, or thermal means. The resulting material, which has been referred to as reduced graphene oxide (RGO),[86,87] has structure and properties somewhere along a spectrum between graphene oxide and pristine graphene, depending on the degree of reduction and starting structure of the graphene oxide. Due to the existence of functional groups and topological defects that differentiate RGO from pristine graphene (see Figure 6 for schematic), the term functionalized graphene sheet (FGS) has also been used as a generic name to label these materials.[78] In addition to RGO and FGS, a plethora of acronyms are already currently in use in the literature (FLG for few-layered graphite[88] or few-layered graphene,[89] GNP for graphene

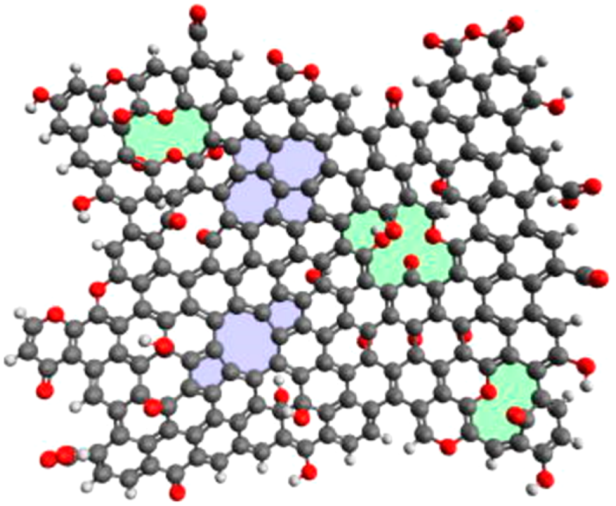

Figure 6. Schematic of functional groups and lattice defects on RGO (termed FGS in the original paper). Carbon atoms are gray, oxygen atoms are red, and hydrogen atoms are white. Some carbon vacancy defects are light green, and topographical defects are light blue. Adapted with permission from *Appl. Phys. Lett.* **2013**, *102*, 023114. Copyright 2013 American Institute of Physics (ref 67).

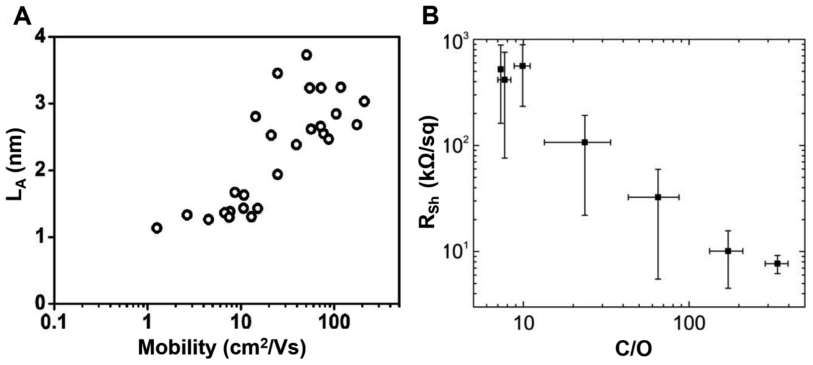

Figure 7. Relations of structural and electrical properties of RGO. (A) Mobility as a function of L_A. Adapted with permission from ref 94. Copyright 2010 American Chemical Society. (B) R_{Sh} as a function of C/O. Adapted with permission from *Appl. Phys. Lett.* **2013**, *102*, 023114. Copyright 2013 American Institute of Physics (ref 67).

nanoplatelets[22] or graphite nanoplatelets,[90] GP for graphene platelets,[91] TEGO for thermally exfoliated graphite oxide,[92,93] etc.). Some of these acronyms refer to the process path followed to form the material, and others refer to the structural and chemical characteristics of the material regardless of the process path followed.

When dealing with a broad spectrum of studies, as in this review, the process path followed to produce the RGO is an important parameter to identify; thus, to maintain uniformity and simplicity between studies analyzed, our priority is to emphasize the specific process path as we describe below. For instance, when a chemical reduction process is used with graphene oxide, we term the material chemically reduced graphene oxide (CRGO). The most prevalent means of chemical reduction of graphene oxide is through hydrazine vapor; however, many other reducing agents have also been used.[41,46,48,52] Both deoxygenation and dehydration reactions can take place, which partially restore the aromatic carbon lattice. Nevertheless, C/O is limited to ~13 in this approach, confining the size of the pristine graphene domains (L_A) in the material and the associated mobility (see Figure 7A).[46,94]

Thermal treatment of graphene oxide—on a substrate, as a powder, or in suspension—will also reduce the material, with higher temperatures and longer durations resulting in higher degrees of reduction. Alternatively, rapid heating of graphite oxide (i.e., putting the material into a furnace heated to 1100 °C) can simultaneously exfoliate and reduce the material, resulting in a black fluffy (vermiculite-like) powder with specific surface areas reported to be above 800 m^2/g measured by nitrogen adsorption. When this vermiculite-like powder is dispersed in a colloidal suspension containing individual graphene oxide sheets, surface areas greater than 1750 m^2/g are measured by dye adsorption methods.[71,78] Although heating in a furnace is most often employed for thermal reduction, other techniques have been explored as well, including microwave heating,[95,96] flash photoreduction,[97,98] and heating in suspension (i.e., solvothermal reduction).[99,100] In this review, all materials created through these techniques are referred to as thermally reduced graphene oxide (TRGO). Thermal treatment of graphene oxide removes oxygen from the material through evolution of CO, CO_2, H_2O, and O_2, leaving behind lattice defect sites when carbon is removed from the lattice.[71,78,101−106] Nevertheless, at elevated temperatures the lattice diffusion rate of carbon is enhanced, and by 1500 °C annealing of the lattice (i.e., increasing L_A) is observed[107] resulting in large increases in conductivity.[67,108] Some researchers use a two-step process of chemical reduction followed by thermal reduction.[85] The idea is to first remove as many oxygen sites without disrupting the lattice as possible and then remove the remaining groups thermally, resulting in a final material with fewer lattice defects than those treated only thermally.[85] This type of material often has electrical properties more similar to TRGO, and in this review, the material is distinguished from CRGO by referring to it as thermally treated CRGO, or T-CRGO.

As can be expected from the different structures, various graphene materials have distinct properties. One of the most prominent transitions is observed in RGO with the conductivity ranging between that of graphene oxide (an insulator) and that of graphene (a semimetal). Conductivity (inverse of resistivity) of a material is equal to the product of its mobility, charge carrier density, and elementary charge. Thus, a material's sheet resistance R_{Sh} is inversely proportional to its mobility and the number of charge carriers. Figure 7 shows the experimentally derived correlations (Figure 7A) between L_A and electron mobility and (Figure 7B) between C/O and R_{Sh} for TRGO. Although mobility increases as graphitic domains grow and become percolated, the number of charge carriers is likely reduced as functional sites are eliminated. At the highest C/O, R_{Sh} is similar to that measured for pristine graphene; however, it is likely that the electron mobilities are higher and charge carriers are lower in the latter case due to the lack of defects in the material.

Another property that is highly dependent on the method and degree of reduction is the electocatalytic activity. The basal plane of graphite, similar to pristine graphene, is known to be relatively inactive for a range of redox couples, while defects and edges, prominent on RGO, are more active.[109,110] These active sites have been used for catalysis as well as to stabilize nanoparticle and molecular attachments.[111,112]

Figure 8 summarizes the production methods for graphene materials. Pristine graphene can be isolated by exfoliation of graphite or grown on substrates. It should be reiterated that RGO materials are not pristine graphene but rather highly defective sheets decorated with oxygen groups (epoxides, hydroxyls, carbonyls, etc.), topological defects, and lattice vacancies (see Figure 6), whose make up is highly dependent on the starting material and reduction parameters. The interior of the triangle represents a phase diagram for RGO materials and depicts the progression of oxygen content and defectiveness (i.e., L_A) for different reduction techniques. Although graphite is the standard feedstock for oxidation and reduction,

dx.doi.org/10.1021/cr400412a | *Chem. Rev.* XXXX, XXX, XXX−XXX

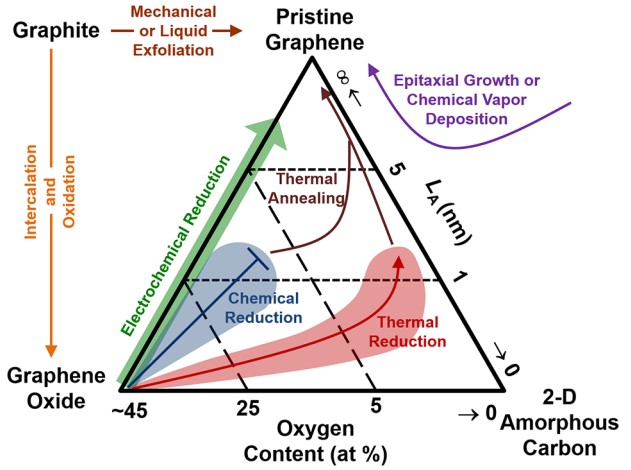

Figure 8. Production of graphene materials. The triangle qualitatively represents the material space encompassed by RGOs. Reprinted with permission from ref 2. Copyright 2013 Joseph Roy-Mayhew.

additional carbon sources (e.g., carbon nanotubes (CNTs), carbon fiber, etc.) can also be used, and these can result in RGO sheets of different aspect ratios and sizes. Another factor that may affect results, but due to a lack of information, whose affect we cannot discern in this review, is the purity of the final materials. Bulk production methods often result in significant amounts of impurities (Mg, K, S, etc.) and multilayered sheets. These can be removed through additional processing steps (i.e., repeated washings, centrifugation); however, these steps are not ubiquitous.

3. PHOTOANODE

The photoanode of a DSSC is made up of a semiconducting layer sensitized by a dye on a conducting substrate. The following three sections focus on the use of graphene materials as transparent conductors (section 3.1), in the semiconducting layer (section 3.2), and as the sensitizer itself (section 3.3).

3.1. Transparent Electrode

Transparent conducting films (TCFs) are required in traditional DSSCs as well as a host of other applications including flat panel displays and touchscreens. Due to this fact, TCFs are often studied independent of a particular device with the primary goal of minimizing R_{Sh} while maximizing transparency (particularly over the visible spectrum). Depending on the desired application, secondary goals can include flexibility, mechanical stability, chemical stability, and catalytic activity.

Indium tin oxide (ITO) is the industry standard TCF, and it can boast R_{Sh} of 5 Ω/sq at ~90% transmittance (T) in the visible spectrum (often reported at 550 nm).[113] Nevertheless, indium is a rare-earth metal, and ITO films are mechanically brittle, not compatible with strong acids, and not stable at high temperatures. FTO, an alternative TCF, is most often used in DSSCs as it is more robust to harsh chemical and thermal treatments (up to ~700 °C) which occur during solar cell fabrication.[114] Although cheaper than ITO, FTO films have higher resistivity per optical absorption, 15 Ω/sq at T ~85%.[113] Detailed reviews on traditional transparent electrodes can be found by Chopra et al. and Gordon.[113,114] To overcome cost and performance limitations of the transparent conducting oxides and to meet the drive for flexible electronics, there has been a strong push to develop alternative TCFs in both academia and industry. Due to the high electron mobility and transparency of single-sheet pristine graphene, graphene materials have been targeted as strong candidates to replace the conductive oxides. Overviews of the major advances and approaches have been recently reviewed in several publications.[51,115−118] As will be described in this section, although pristine graphene is unlikely to meet industrial targets for high-performing devices, electronically doped graphene materials and graphene−metal hybrid materials have already shown strong promise as transparent electrodes. We provide a synopsis of the major fabrication techniques and performance milestones, starting with approaches using only graphene materials as TCFs and then follow up on this with hybrid material approaches. Lastly, specific uses of TCFs in DSSCs are reviewed.

Each layer of graphene absorbs about 2.3% of light; thus, for 90% transmittance, light can pass through a maximum of ~5 sheets.[51] Single-sheet measurements show that TRGO sheets with C/O above 300 (i.e., highly reduced material) have R_{Sh} of ~7.7 kΩ/sq (Figure 7B),[67] while that for pristine graphene is ~6.45 kΩ/sq,[66] suggesting that layers of the material can only achieve R_{Sh} around 1 kΩ/sq for T = 90%, even before accounting for contact resistances between individual sheets. In 2008, Wang et al. were the first to report on using a graphene material as a TCF, and they used the film as the window electrode (the electrode through which light enters) in a DSSC.[26] These TRGO films were formed by sequential dip coating of graphene oxide onto silica glass and then annealing the films at 1100 °C. High-temperature processing was required in order to reduce the material sufficiently, increasing the size of sp^2-hybridized aromatic networks (i.e., L_A) and increasing conductivity as described in section 2. Those characterized for use as DSSC window electrodes were about 10 nm thick and had R_{Sh} = 1.8 kΩ/sq and T = ~62% at 550 nm. Although far from the performance achieved with FTO and lower than could be expected from single-sheet measurements, these cells demonstrated the proof of concept for the use of graphene materials as a transparent conductor and inspired many studies to advance this work. For instance, Becerril et al. spin coated thin layers of graphene oxide onto silica glass and reduced the films through different methods including hydrazine treatment and thermal annealing at 1100 °C.[119] They found that thermal annealing resulted in films which were over an order of magnitude less resistive than chemically reduced films at a given transparency, a result likely due to the higher degree of reduction achievable with thermal processing. However, their TRGO films still had an R_{Sh} of ~1 kΩ/sq at T = 80%. Zheng et al. were able to improve significantly on these results by creating large area graphene oxide (up to ~200 μm diameter sheets) and forming thin films through a Langmuir−Blodgett trough approach.[116] Large sheets are beneficial in reducing the number of boundaries and thus contact resistance of the tiled mosaic film, bringing the TCF closer to what could be achieved by a continuous graphene sheet. After high-temperature annealing, an R_{Sh} of ~600 Ω/sq was obtained at T = 90%, a value better than would be expected from the single-sheet measurements, but still almost 2 orders of magnitude higher than achievable with ITO.

De and Coleman analyzed over 20 studies of graphene material-based transparent electrodes and suggested a way to standardize the comparison of the various techniques.[115] This method relates the conductivity and transmittance of the material through the ratio of the dc conductivity (σ_{DC}) to the optical conductivity (σ_{Op}). The ratio can be then related to

dx.doi.org/10.1021/cr400412a | Chem. Rev. XXXX, XXX, XXX−XXX

electrode properties through $T = (1 + ((z_0/(2R_{Sh})))((\sigma_{Op})/(\sigma_{DC}))^{-2}$, where Z_0 is the impedance of free space (377 Ohm). Their analysis showed that RGO (they term flakes) are severely limited by contact resistance between sheets (σ_{DC}/σ_{Op} limit of 0.7), with larger sheets (such as achieved the Zheng et al. approach or by CVD methods) achieving higher conductivity due to fewer contact regions. For reference, to achieve a 100 Ω/sq film at T = 90%, σ_{DC} /σ_{Op} must be 35 or greater. Through their calculations, CVD-derived graphene is more suitable than a mosaic of sheets (σ_{DC}/σ_{Op} limit of 2.6), but it is still far from meeting commercial needs.

Nevertheless, De and Coleman note that conductivity limits can be greatly increased by increasing the carrier concentration through substrate interactions or electronic doping,[115] an idea which follows from the fact that conductivity is equal to the product of a material's electron mobility, its charge carrier density, and the elementary charge. As previously discussed in section 2, electron mobility is correlated to the size of the aromatic domains, with highest values obtained for pristine graphene. Yet, the charge carrier density of pristine graphene is low, resulting in an R_{Sh} similar to that of the RGO material.[66] Thus, in order to meet the performance of conventional TCFs, increasing the charge carrier density of the graphene materials is necessary. Electronic doping can occur through incorporation of electron-donating or -accepting species into the graphene lattice or more commonly through adsorption of these species on sheets. Both HNO_3 and $SOCl_2$ are common examples of chemicals used for the latter electronic doping method. By electronic doping, Zheng et al. decreased R_{Sh} in their TRGO films almost 25% to 459 Ω/sq at T = 90%, a significant improvement but still over an order of magnitude more resistive than ITO films.[116] Bae et al. were able to create industrially relevant TCFs by stacking four monolayers of CVD−graphene and then electronically doping the film with HNO_3.[120] These films, which measured 30 in. (0.76 m) along the diagonal, exhibited an $R_{Sh} \approx$ 30 Ω/sq at T = 90%. Further improvements to mobility or charge carrier concentration could further decrease the resistance.

Alternative approaches to achieve high performance have included forming hybrid materials. For instance, both [CVD-derived graphene]−CNT,[121] and CRGO−CNT[122] hybrid films have been produced, as have CRGO−[silver nanoparticle] hybrid films.[123] The best performance to date of graphene-based TCFs has been with [CVD-derived graphene]−[metal nanowire] films. Through photolithography, Zhu et al. created metal nanogrids (Au, Cu, and Al) with grid lines 100 nm thick and 5−10 μm wide, spaced 100−200 μm apart.[124] CVD-derived graphene was then used to coat the grid and form a continuous conductive network. In this case, the relatively thick metal grids act as the primary current collector reducing the need for graphene materials with super high mobility and charge carrier density. Using grid boxes smaller than the grain size of the CVD-derived graphene, which has been shown to be dependent on the grain size of the metal substrate, i.e., copper, potential high-resistance zones can be avoided. As charge is supposed to be transferred from the graphene material (which covers much more of the surface than the metal) to the metal grid the contact resistance between these materials becomes important with this system. Nevertheless, these hybrids have reached R_{Sh} of ~3 Ω/sq at T = 80% or ~20 Ω/sq at T = 90%.[124] Figure 9 provides an overview of what has been achieved for graphene-based TCFs.

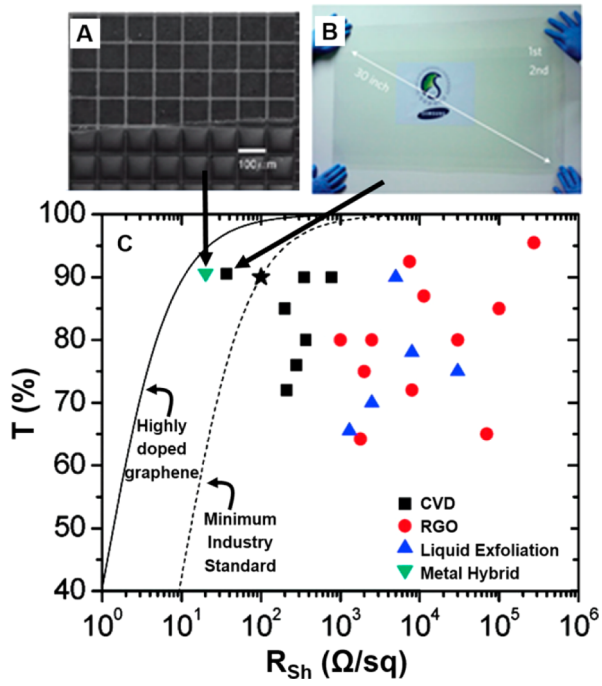

Figure 9. Overview of graphene materials in transparent electrodes. (A) Metal grid coated with CVD-derived graphene film. Adapted with permission from ref 124. Copyright 2011 American Chemical Society. (B) Large area HNO_3 electronically doped CVD-derived graphene film. Adapted by permission from Macmillan Publishers Ltd. *Nature Nanotechnology* from ref 120, copyright 2010. (C) Compilation of transparent films. Adapted with permission from ref 115. Copyright 2010 American Chemical Society. Dotted line represents σ_{DC}/σ_{Op} = 35, with the star representing R_{Sh} = 100 Ω/sq at T = 90%. The solid line represents σ_{DC}/σ_{Op} = 330, a value calculated for highly electronically doped pristine graphene.

Even though Wang et al. first reported graphene as a DSSC window electrode, further reports in this application have been scarce. Bi et al. demonstrated the growth of CVD-derived graphene directly on silica glass substrates and used these as the current collector at the cathode of a DSSC (light entered the cell through the anode).[125] However, the devices were hindered due to the relatively high R_{Sh} compared to FTO (1449 Ω/sq at T = 79.5% and 63 Ω/sq for opaque films). Both Cottineau et al. and Wu et al. studied how to electrodeposit metal oxides onto mechanically exfoliated graphene and CRGO, respectively.[126,127] Although these films were not employed in a solar cell, the approaches developed represent a first step toward creating thin film, flexible photocathodes for DSSCs.

As researchers have fabricated graphene-based transparent electrodes with R_{Sh} < 30 Ω/sq at T = 90%, approaching the performance of conventional FTO and ITO electrodes, it is evident that graphene electrodes can enter the market. However, it is not clear if they will do so and if so when. The scalability of the technology and cost reductions must be demonstrated to be used in commercial devices. With regard to DSSCs, extra constraints may arise depending on the electrolyte and solar cell design. For instance, metal hybrid electrodes would likely corrode in an iodine-containing electrolyte. In any case using graphene materials in transparent electrodes is far from mature, and more advances will be made, particularly for applications in which the current TCFs do not work well, such as low-temperature substrates and flexible devices.

dx.doi.org/10.1021/cr400412a | *Chem. Rev.* XXXX, XXX, XXX−XXX

3.2. Semiconducting Layer

In a DSSC, a photoexcited electron is injected from the dye into the semiconductor where it diffuses to the current collector. Losses occur for several reasons including due to the voltage drop between the dye LUMO level and the Fermi level of the semiconductor, from the ohmic resistance in the semiconducting layer, and from recombination of injected electrons with the dye or with oxidized species of the redox couple. In this last case, electrons from the semiconductor or from the current collector (i.e., FTO) can recombine with the electrolyte. Many techniques have been developed to minimize these losses. For instance, anatase phase TiO_2 energy levels match favorably with many dyes, providing injection efficiencies near unity,[128−130] with acceptable voltage drop. Moreover, it has been shown that TiO_2 has a low recombination rate with triiodide (of the common iodide/triiodide redox mediator); thus, dense layers of TiO_2, ∼20−100 nm thick, are often used as a blocking layer to prevent recombination from FTO to triiodide.[131−133] Lastly, TiO_2 has a relatively high conductivity for a semiconductor due in part to oxygen vacancy n-doping and photoexcitation of electrons in the material. It has been shown that crack-free, sintered films optimized for DSSCs can exhibit electron diffusion lengths significantly longer than the film thickness itself, resulting in near unity charge collection efficiencies.[134−136] The film thickness (generally 10−20 μm) is chosen in order to have adequate light harvesting and is determined by the surface area of the semiconducting scaffold and the extinction coefficient of the dye.

Although best practices are widely disseminated, only a few laboratories have been able to create DSSCs with efficiencies of over 10%, providing a testament to the difficulty in replicating these best-in-class devices. Thus, as an alternative approach, many groups have sought to use graphene materials to improve the performance of the semiconducting layer in DSSCs. Below, we first describe the use of graphene materials in the blocking layer to prevent recombination between the FTO and triiodide. Then we discuss the use of graphene materials in the TiO_2 scaffolding to improve photocurrent density and explore the rationales provided (e.g., improved electron transport, dye adsorption, and light scattering) for the observed improvements. We reiterate that best-in-class devices have overcome many of the limitations arising from FTO recombination and TiO_2 charge transport without using graphene materials; however, we cannot rule out that the techniques described in this section could provide a more commercially feasible way of achieving similar results.

To our knowledge, the first use of a graphene material in the semiconducting layer of a DSSC was reported by Kim et al., who used a photocatalytically reduced graphene oxide−TiO_2 nanoparticle composite (TiO_2 particle diameter < 10 nm) as a blocking layer with the idea that the flat sheets could be deposited at low temperatures and without dangerous chemicals, unlike the common $TiCl_4$ treatment, and that they would provide a barrier between triiodide and FTO.[137] The group demonstrated a 7.6% relative improvement in efficiency over a cell without a blocking layer. However, due to significant light absorption from the film (T decreased from 85% to 78%) and potential catalysis of triiodide reduction (see section 5), their approach does not seem to be more beneficial than the traditional TiO_2 blocking layers. Several other studies used similar approaches[29,34,138] and also saw improvements. For instance, Chen et al. spin coated thin layers of TRGO as a blocking layer, resulting in an 8.1% efficient cell, which was better than a cell without a blocking layer (η = 7.2%) and better than one with their $TiCl_4$ pretreatment blocking layer (η = 7.5%). The improvement was due to an increase in photocurrent.[29] Interestingly, the blocking layer only absorbed 1.6% of light, suggesting that, on average, less than a monolayer of TRGO was present or that the TRGO was only slightly reduced, resulting in a less absorbing material. Graphene oxide would provide a barrier for electron recombination with the FTO, but it would also provide an insulating barrier, so only very thin layers which allowed tunneling could be effective. Furthermore, graphene materials can only work effectively for a blocking layer if they are less active for the redox mediator than FTO is. Although this is likely the case with the triiodide mediator, and hence the improvement reported, it is not universally the case (for instance, graphene materials are highly active for the $Co(bpy)_3$(II/III) couple, where bpy is bipyridine, see section 5).

A more established use of graphene materials has been their incorporation into the semiconducting layer itself.[28,29,31−34,138−147] A driving motivation for this work was to increase device performance through increasing charge collection efficiency, i.e., photocurrent, in the photoanode. A typical DSSC has a 10−20 μm thick layer of TiO_2. Thus, electrons photogenerated in the rear of the device have to diffuse to the front to be collected, a length on the order of 100 μm assuming a random walk. The collection efficiency as a function of electron diffusion length and film thickness can be approximated by examining electron transport and electron recombination time scales as shown in Figure 10.[148]

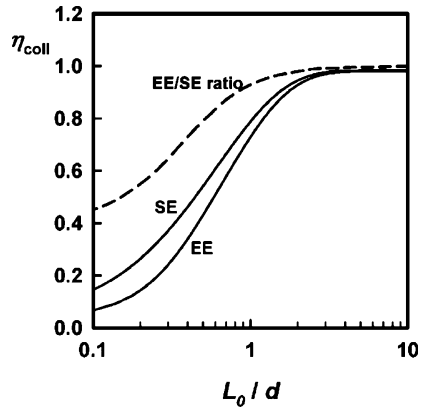

Figure 10. Charge collection in the photoanode. η_{coll} is the charge collection efficiency, the SE curve represents collection when the device is illuminated from the front (through transparent conductor), while EE represents illumination from the rear (though counter electrode and electrolyte). L_0 is the path length to the current collector, and d is the electron diffusion length in the material. Thus, using this model, an electron generated 10 μm from the current collector in a TiO_2 film which had a 20 μm diffusion length would reach the current collector about 90% of the time (∼10% of the electrons would recombine). Reproduced with permission from ref 148. Copyright 2009 American Chemical Society.

One method to increase collection efficiency is to improve electron transport in the TiO_2 (i.e., increase the diffusion length), as is done with the sintering process. An alternative method is to decrease the electron path distance, which can be done by creating finger electrodes into the TiO_2 layer as reported by Chappel et al. and later by Joanni et al.[149−151] A schematic of the approach can be seen in Figure 11. In these

dx.doi.org/10.1021/cr400412a | Chem. Rev. XXXX, XXX, XXX−XXX

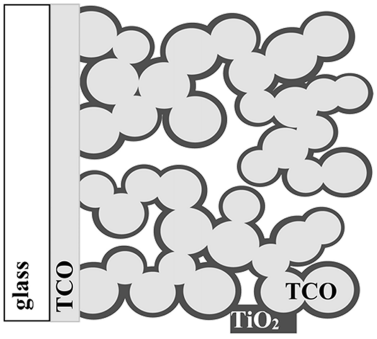

Figure 11. Schematic of a nanoporous transparent conducting oxide (TCO) acting as the electrode to reduce the collection length. Most of the volume is taken up by the TCO, limiting the amount of TiO_2 and surface area available for dye adsorption. Reproduced with permission from ref 150. Copyright 2005 American Chemical Society.

studies, the approach was significantly limited by the primary particle size of tin oxide or ITO used in the electrode material as well as by the need to coat the conducting fingers with a blocking layer of TiO_2 (at least 6 nm) to prevent recombination in the device.[150] Graphene materials hold a distinct advantage here due to their atomic thinness and high aspect ratio which provide a low percolation threshold.[152] Ideally, they could act as a current collector with only slight changes to the TiO_2 film morphology. For best results, a conductive graphene material should be used which has minimal defects for catalytic activity (see section 5) or which can be effectively coated by a dense TiO_2 layer. As described below, several studies have used graphene materials to this effect, with between 0.5 and 1.0 wt % inclusion of the material providing the best results. Although some studies report increased TiO_2 conductivity as the primary cause for improvement, others claimed it was due to unforeseen side effects such as increased dye loading and light scattering in the electrode. The following section treats each of these effects in turn.

The first study on this topic was published in 2010, in which Yang et al. argue that graphene can act as an electron bridge in the photoanode, shuttling electrons to the current collector and lowering recombination in the device.[28] Unlike in the schematic above, there was no attempt to completely coat the conductor with the semiconductor. Nevertheless, in this work, they saw an increase in device efficiency from 5% to 7% by first adding 0.6 wt % CRGO into the TiO_2 particle film (commercial P25 particles) and then heating the composite to 450 °C to sinter the TiO_2 and further reduce the CRGO. The improvement was solely the result of increased photocurrent. Since then over a dozen studies reproduced this effect and tried to elucidate the improvement mechanism. Results from these studies are tabulated in Table 2, and device efficiencies are compared to control cells in Figure 12. In studies where several compositions were tested only the top performing case was included. The authors discussed several means of improvement to explain these results. At least five studies reported that adding graphene materials to the TiO_2 layer resulted in an increase in dye

Table 2. DSSC Performance of Devices with Graphene Materials in the TiO_2 Layer Compared to Control Cells

sample	graphene material content[a] (wt %)	J_{SC} (mA/cm^2)	V_{OC} (V)	*FF*	η (%)	ref
control	0	2.0	0.52	0.31	0.4	139
underlayer with T-CRGO	0.04[b]	6.7	0.56	0.45	1.7	
control	0	11.3	0.69	0.65	5.0	28
scaffold layer with T-CRGO	0.6	16.3	0.69	0.62	7.0	
control	0	9.6	0.82	0.62	4.9	32
scaffold with thermally treated CTAB-functionalized graphene	0.5	12.8	0.82	0.62	6.5	
control	0	5.0	0.66	0.55	1.8	33
scaffold layer with TRGO	0.83	7.6	0.67	0.54	2.8	
control	0	10.2	0.71	0.70	5.1	34
scaffold layer with TRGO (solvothermal)	0.8[b]	13.2	0.72	0.73	7.1	
control	0	13.7	0.59	0.57	4.6	123
scaffold layer with RGO	0.75	16.8	0.61	0.57	5.8	
control	0	9.8	0.77	0.61	4.6	140
scaffold layer with CVD-derived graphene on Al_2O_3	1[c]	10.2	0.78	0.68	5.4	
control	0	18.8	0.68	0.56	6.0	141
scaffold layer with unknown graphene material	1	19.9	0.70	0.49	6.9	
control	0	5.0	0.74	0.71	2.7	144
scaffold layer with T-CRGO	0.5	8.4	0.75	0.68	4.3	
control	0	8.7	0.77	0.66	4.4	156
scaffold layer with CRGO	1	12.9	0.68	0.69	6.1	
control	0	15.2	0.71	0.53	5.8	29
scaffold layer with CRGO	0.02	16.5	0.75	0.58	7.2	
$TiCl_4$-derived undercoat, scaffold layer with CRGO	0.02	19.3	0.74	0.53	7.5	
underlayer with TRGO, scaffold layer with CRGO	0.02	19.5	0.75	0.56	8.1	
control (including $TiCI_4$-derived underlayer, $TiCl_4$-derived overcoat, and scattering layer)	0	13.3	0.77	0.76	7.8	170
scaffold layer with graphene oxide	0.8	13.6	0.76	0.75	7.7	
control	0	14.9	0.71	0.59	6.3	138
underlayer with RGO, scaffold layer with RGO, scattering layer with RGO	5	23.2	0.73	0.55	9 2	

[a]Prethermal treatment. [b]Calculated from data in paper. [c]Mass of Al_2O_3 and graphene material.

dx.doi.org/10.1021/cr400412a | *Chem. Rev.* XXXX, XXX, XXX−XXX

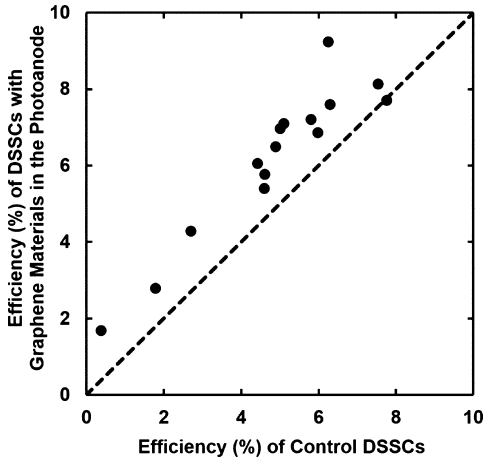

Figure 12. Comparison of reported efficiencies for DSSCs with and without graphene materials in the TiO_2 scaffold layer.

absorption,[32,139,141,142,144] which in turn increased the light-harvesting efficiency and accounted for an increase in photocurrent. However, other studies did not see a change in dye absorption,[28,33,138] and some reported a lower absorption,[29,140,153] even though all of these studies report a higher photocurrent.

The study by Yang et al. also reported that inclusion of RGO induced formation of macropores in the TiO_2 films which acted to scatter light.[28] The authors state that this effect could be responsible for up to 7% of the 39% increase in photocurrent observed. Fang et al. hypothesized that porosity was due to voids formed from the reduction in volume of graphene oxide during heating.[147] At elevated temperatures, graphene oxide becomes dehydrated and residual oxygen groups are removed. Although the width of RGO is about one-half that of graphene oxide, this change is on the nanometer scale and thus cannot be responsible for the reported light scattering, an effect that would require macroscopic porosity. An alternate explanation would be that including RGO in the system affected the rheology of the paste (likely greatly increasing the viscosity), preventing smooth and dense film deposition. Furthermore, Durantini et al. found that a [solvothermally reduced graphene oxide]−TiO_2 composite absorbed 44% more light at the dye's (N719) absorption peaks (~370 and ~500 nm), which could explain the full increase in photocurrent in their study (29%).[34] Although they attributed this result to light scattering, the authors also mentioned that they could not rule out other optical effects, such as the TRGO acting as a sensitizer itself. Besides direct sensitization (for more direct studies on this see section 3.3), enhanced light harvesting could be due to increased absorption in TiO_2. In photocatalysis studies, it has been shown that the presence of graphene materials can reduce the band gap of TiO_2 into the visible spectrum, speculatively through Ti−O−C bonding,[154,155] and Peining et al. report a 25 nm red shift in absorption for a TiO_2 film incorporating thermally annealed CTAB-functionalized graphene.[32] Even more surprising is the report of the shifting of the TiO_2 band gap to 2.11 eV (588 nm) with inclusion of 1 wt % CRGO.[156]

Increased dye absorption and scattering contribute to improved performance; nevertheless, based on electrochemical impedance spectroscopy (EIS) data, Yang et al. proposed that increased collection efficiency was primarily responsible for their observed increase in performance.[28] Many studies have looked into how to interpret EIS spectra for DSSCs.[157−163] EIS provides information on interface resistances (and capacitances) in electrochemical systems. For DSSCs, this can include the series resistance of transport through the current collector (R_S), charge transfer resistance (R_{CT}) at the cathode/electrolyte interface, resistance between the TiO_2 particles (represented by a transmission line model), TiO_2/electrolyte recombination resistance (R_R), and diffusion resistance (Z_D). A simple resistor in parallel with a capacitor, such as is the case for the cathode/electrolyte interface, is represented by an arc in a Nyquist plot, while the transmission line arises as a diagonal line at high frequencies. These features can be seen in Figure 13. It is

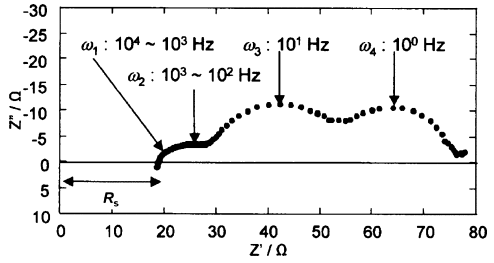

Figure 13. Sample EIS spectra of full DSSC under light. Often, as a result of DSSC fabrication techniques, only two of these features can be discerned during testing. Adapted from *J. Electrochem. Soc.* **2005**, *152*, E69. Copyright 2005 ECS-The Electrochemical Society (ref 157).

important to note that the interpretation of EIS data is only as good as the equivalent circuit used, with the most widely used models shown in Figure 14 (Figure 14A is in the dark; Figure 14B is in the light, where TiO_2 becomes more conductive due to increased electron density).

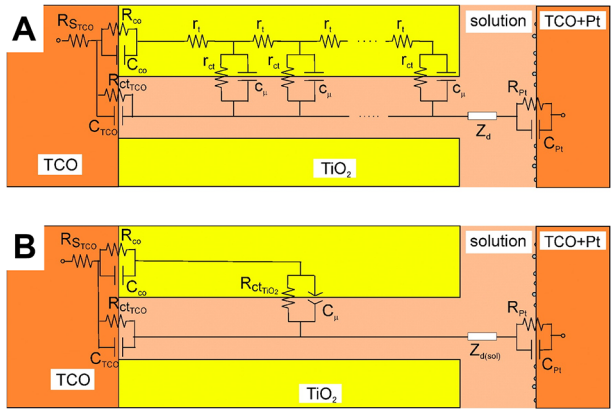

Figure 14. EIS equivalent circuits for DSSCs (A) in the dark and (B) under illumination. Reproduced with permission from ref 162. Copyright 2007 American Chemical Society.

In addition to the magnitude of resistances, the characteristic frequency that a resistance is observed at can provide insight into electron transport. For instance, the electron lifetime, and from this the diffusion length, can be approximated from the characteristic frequency of the TiO_2/electrolyte interfacial resistance arc, where frequency is proportional to the inverse of the electron lifetime.[161] However, depending on the materials used and how the device is fabricated, spectra for various resistances may overlap in frequency and the interpretation is less clear without additional measurements. This overlap is especially important when evaluating the photoanode as the resistance between TiO_2 particles (trans-

dx.doi.org/10.1021/cr400412a | *Chem. Rev.* XXXX, XXX, XXX−XXX

mission line) and the resistance of the TiO_2/electrolyte interface occur at similar frequencies and thus have an ambiguous interpretation.[158,161] Unfortunately, this ambiguity is often ignored in the publications, and it is aggravated by the fact that the resistance between TiO_2 particles should be minimized and TiO_2/electrolyte resistance should be maximized (shunt resistance) in high-performing DSSCs.

Yang et al. see two semicircles in their impedance spectra as displayed in a Nyquist plot.[28] They assign the high-frequency semicircle to R_{CT}, which is consistent with a large body of literature for using platinum counter electrodes (see section 5 for more details). They then claim that a lower resistance at midfrequencies represents improved electron transport in the film. The characteristic frequency of this arc is also shifted, which they interpret to be representative of the electron lifetime. Chen et al. made a similar analysis with 0.02 wt % CRGO incorporated into their TiO_2 film,[29] as did at least 10 other studies.[31,33,138−145] However, another body of work sees an increase in the middle frequency semicircle upon inclusion of graphene materials, which they claim to be due to R_R. Thus, for these works, the authors report that a larger resistance represents a decrease in electron recombination to the electrolyte and higher collection efficiency.[32,34,146,147] This interpretation is supported by the most extensive EIS studies for TiO_2 films. With appropriately sintered TiO_2, the resistance between TiO_2 particles is seen primarily in the dark, and R_R dominates under illumination due to the photoconductivity of TiO_2.[34] In a detailed EIS study undertaken at various bias potentials and using a DSSC equivalent circuit developed by the Bisquert group, it was determined that the photocurrent improvement was not due to a reduction in recombination nor from a shift in the Fermi level.[34] Under light, the TiO_2 film conductivity was too high to measure, suggesting R_R to be negligible, in agreement with previous studies on the photoconductivity of the TiO_2 layer.[160,164,165] With this interpretation, a decreased midfrequency semicircle could represent greater recombination, perhaps caused by graphene materials acting as recombination centers due to their activity toward triiodide reduction (see section 5). This recombination could be minimized by effectively coating the sheets, or networks of sheets, with TiO_2 as was attempted for the FTO finger electrodes.

Some groups have used graphene materials for both of the roles discussed above, showing successive improvements. Chen et al. used CRGO in the blocking layer and in the TiO_2 scaffold layer,[29] while Tang et al. incorporated CRGO in the blocking, scaffold, and scattering layer leading to a much more efficient device (η = 9.24% compared to 6.25% for a device with just a TiO_2 scaffold layer).[138] In a relatively backward approach, Song et al. coated the top of the TiO_2 layer with CRGO (FTO−TiO_2−CRGO structure) and reported an improvement in photocurrent and efficiency over control samples as well,[153] an improvement which is not adequately justified in the work and cannot be explained by the authors of this review. How these devices would compare to those optimized with current best practices for blocking, scaffold, and scattering layers is unknown, but it is clear that the performance increase, if any, would be greatly diminished.

Graphene materials have been incorporated into the semiconductor film in a variety of ways including grinding of powders,[166] ball milling,[147] colloidal aggregation,[34] and coelectrospinning.[32] To prevent sheet aggregation, Park et al. claim to first coat Al_2O_3 with graphene oxide and then mix these coated particles in with TiO_2, where they are then heat treated.[140] This approach requires a large fraction of inactive material (aluminum oxide) in the DSSC. Similarly, Li et al. saw improvements in DSSCs with a TRGO−YF4:Er^{3+}/Yb^{3+}− composite mixed into TiO_2,[167] though it is unclear why this system was chosen. Lastly, in addition to the traditional TiO_2−dye DSSCs described above, graphene materials have been incorporated into quantum dot photochemical cells[142,168] and in p-type DSSCs.[169] In the latter case, the conductive properties may play a much larger role due to the low conductivity of NiO which is used as the dye scaffold and hole conductor. In almost all approaches described, whether the initial material was graphene oxide, CRGO, or TRGO, the cells underwent sintering conditions at temperatures between 300 and 500 °C resulting in an RGO material. Because of this, as the paper by Wang et al. illustrates, it may not be necessary to start with RGO. Processing graphene oxide, which is readily water dispersible, rather than RGO, could simplify hybrid photoanode fabrication.[33]

It is clear that graphene materials can play a variety of roles in the semiconducting layer of a DSSC photoanode and that addition of these materials can improve a poor or mediocre device's performance. Nonetheless, it is still unclear whether addition of graphene materials into best-in-class cells would have an improvement. In these optimized devices, TiO_2 blocking and scattering layers are effective at reducing recombination and increasing light harvesting, respectively. Furthermore, TiO_2 films can be fabricated without cracks, and they can be sintered to provide a highly photoconductive network. In these devices, electron diffusion lengths have been measured to be much larger than photoanode thicknesses and collection efficiencies near unity are reported. One study, by Neo and Ouyang, suggests that improvements may not be realized for cells which have undergone further optimization such as we have described. In their work, graphene oxide was used as an auxiliary binder and 13 μm thick crack-free films were able to be formed from a single doctor bladed layer, rather than the four layers typically required with commercial pastes.[170] The cells were then heat treated, sintering the TiO_2 and reducing the graphene oxide. In these devices, which employed TiO_2 blocking and scattering layers, the performance of devices made with and without TRGO was nearly identical (η = 7.70% and 7.76%, respectively). In line with this work and the results presented above, it is the opinion of the authors of this review that incorporating graphene materials into the photoanode will not improve upon current best practices, though it could provide an alternative method of achieving the same goals.

3.3. Sensitizer

An effective sensitizer for a DSSC must be able to absorb a significant portion of the solar spectrum and be able to inject excited electrons into a semiconducting scaffold faster than they relax to the sensitizer's ground state. As previously mentioned, N719, one of the most prevalent dyes, absorbs wavelengths up to ~800 nm and has an extinction coefficient of ~1.5 × 10^4 M^{-1}·cm^{-1} (at 535 nm).[4] It achieves near unity charge transfer into TiO_2 due to chemisorption of the dye's carboxylate groups onto the TiO_2 surface, facilitating electron injection.[3] As reviewed in detail by Hagfeldt et al.,[3] researchers have synthesized thousands of dyes with the goal of increasing light harvesting and reducing recombination in the solar cell. Pristine graphene is known to have a broad and strong

dx.doi.org/10.1021/cr400412a | Chem. Rev. XXXX, XXX, XXX−XXX

absorption profile, absorbing about 2.3% of light with each monolayer of material;[69] thus, it has received interest as a possible sensitizing material.

A few studies add credence to this possibility as they report that efficient charge injection from graphene materials to TiO_2 can occur and that graphene can act as a photosensitizer. However, graphene materials have shown poor performance to date in this role. Nevertheless, they have recently shown promise in hot injection[171] and multiple carrier generation,[172] providing a means to surpass the Shockley–Quiessar efficiency limit inherent to current device structures.

Long et al., using nonadiabatic molecular dynamics formulated within the framework of time-domain density functional theory, showed that photogenerated electrons can be transferred from graphene to TiO_2 about 3–5 times faster than they would recombine in the material through relaxation.[173] The ultrafast injection was due to electronic coupling between graphene and TiO_2, with the surface oxygen atoms of TiO_2 forming bridge structures to the graphene sheets. Similar results were obtained by Du et al. using density functional theory calculations to look at injection in the (110) surface of rutile TiO_2. Recently, Williams et al. determined that photoexcited graphene quantum dots (GQDs) inject electrons into TiO_2 with a time constant below 15 fs, suggesting that hot injection (wherein charge carriers are injected before being thermally equilibrated to the conduction or valence band) may be possible.[171] In addition to being able to transfer charge into TiO_2, Zhang et al. experimentally demonstrated that graphene materials (TRGO, hydrothermal method) can act as a photosensitizer.[174] This work discounted the possibility that TRGO only acted to narrow the band gap of the semiconductor (see section 3.2 for further discussion of this).

Putting these ideas into practice, Yan et al. fabricated the first DSSC using graphene material photosensitizers.[27] This device used GQDs which ranged from ~1 to 30 nm in diameter and had an absorption maximum at 591 nm and an extinction coefficient of 1.0×10^5 $M^{-1}\cdot cm^{-1}$, almost an order of magnitude higher than N719. Additionally, the HOMO level was determined to be below the iodide/triiodide redox potential, while the LUMO level was above the TiO_2 conduction band, suggesting that both electron injection and dye regeneration are possible, see Figure 15A. A later study by the same group showed that the GQD band gap can be tuned by controlling the size of the molecule and that the redox potential can be tuned by changing its functionalization.[175] Furthermore, they show that the effect can be predicted through tight-binding calculations and provide a route to design sensitizers with specific properties. Although important as proof of concept devices, DSSCs using GQDs recorded poor performance (η = 0.06%, Figure 15B) due primarily to very low photocurrents, which can be at least partially attributed to poor adsorption of the GQDs onto the TiO_2.[27] Potentially addressing this issue, Hamilton et al. have shown that the orientation of GQDs can be controlled for monolayers by tuning the edge functionalization (Figure 15C).[176] The group was able to achieve horizontal or edge alignment of the GQDs using a Langmuir–Blodgett trough setup. If this result could be made applicable to porous TiO_2 surfaces then light-harvesting problems seen in the earlier DSSC work could be reduced. In the case of edge-aligned GQDs, the charge transfer would have to be examined, as previous simulations assumed a horizontal alignment.

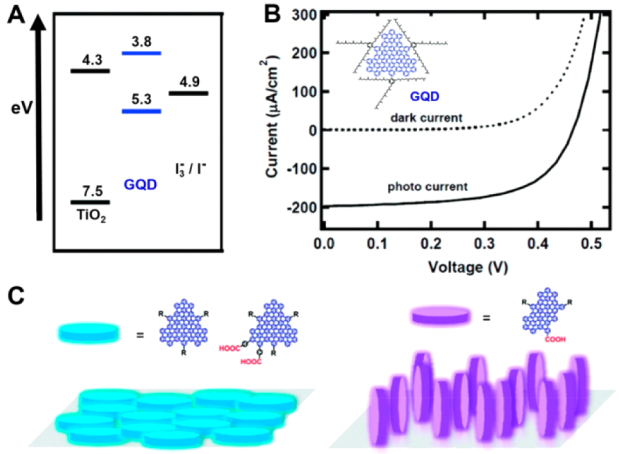

Figure 15. GQD photovoltaic performance. (A) Energy level diagram versus the iodide/triiodide redox couple and anatase phase TiO_2. (B) Photovoltaic performance of a GQD-sensitized DSSC. (Inset) Structure of the GQD used for sensitization. (A and B) Adapted with permission from ref 27. Copyright 2010 American Chemical Society. (C) Schematic of vertical and horizontal orientation of GQDs. Reproduced with permission from ref 176. Copyright 2011 American Chemical Society.

Although graphene materials can be used as a light absorber in DSSCs, the more the structure is optimized (smaller, specific functionalities, etc.) the more it appears to approach traditional organic dyes that have been synthesized. An as of yet unrealized advantage of graphene materials as sensitizers is the possible large-scale production of the product through top-down procedures such as the oxidation and reduction of carbon fibers,[177] nanographite,[178] CNTs,[179] or carbon black, rather than an expensive bottom-up synthesis currently employed for most dyes. Lastly, perhaps the largest role of graphene materials as a DSSC sensitizer would be in a scenario which took advantage of the quantum effects and allowed for ultrafast injection in order to overcome intrinsic limitations to conventional devices.

4. ELECTROLYTE

To achieve efficient dye regeneration and charge carrier transport in DSSCs, a liquid electrolyte with an appropriate redox couple is most often used. For maximum efficiency, this electrolyte would (i) be electrochemically stable over the potential range experienced in a DSSC, (ii) be visibly transparent, (iii) have minimal potential losses due to the mismatch between the dye HOMO level and the electrolyte redox potential, and (iv) have fast charge transport, i.e., small redox species and low-viscosity solvent. For long-term stability, the electrolyte should be nonvolatile. Unfortunately, a solvent's viscosity and volatility are generally inversely related, complicating development of commercial DSSC with high efficiencies. To address some of the limitations of electrolyte systems, a few groups have incorporated graphene materials into the electrolyte of a DSSC.

Approaches for using graphene materials in the electrolyte can be split into two main categories: those using graphene materials as minor additives and those using them as a main constituent (>1 wt %). In the former case, which is discussed first, the authors report gelation of the electrolyte and a bleaching of the electrolyte, both results which could be intriguing to try with high-performance solar cells. A few

dx.doi.org/10.1021/cr400412a | Chem. Rev. XXXX, XXX, XXX–XXX

electrolyte studies fall into the latter case, in which researchers attempt to use graphene materials in high concentrations as conductive fillers to decrease the electrolyte resistance. Although this has been reported to be effective in a few publications, it is easy to find disadvantages to this approach which makes it unlikely to impact DSSC development.

The most practical application of graphene materials in the electrolyte comes from using it as a minor component. Velten et al. found that addition of ~0.005 wt % (~0.04 mg/mL) of graphene nanoribbons (created through oxidation and reduction of CNTs) can lead to a decrease in the optical absorption of the iodide/triiodide electrolyte when under illumination.[180] This phenomenon is explained through the electron transfer from the graphene nanoribbon to triiodide, resulting in less absorbing species. As the iodide/triiodide electrolyte absorbs light (primarily between 350 and 400 nm), its use in DSSCs limits photocurrent generation,[181] especially in inverted architectures where light must pass through the electrolyte bulk before it reaches the photoanode. Using graphene nanoribbons in the electrolyte, Velten et al. showed a 22% increase in efficiency for devices with the inverted architecture (from η = 5.8% to 7.0%), with similar device performance to control cells for noninverted devices (η = 8.5% and 8.4%), see Figure 16.[180]

Also using a graphene material as a minor component of the electrolyte, Gun et al. found that addition of graphene oxide could yield a gel in a range of solvents containing an ionic liquid.[182] Depending on the solvent, the amount of graphene oxide required to form an aggregated network and thus trap the solvent varied from 0.4 to 1.6 wt % as can be seen in Table 3. In their work, a microelectrode study comparing gelled and nongelled electrolytes showed a negligible decrease in diffusion resistance and slight decrease in counter electrode activity with increasing graphene oxide content. Although no long-term device performance was reported, initial results showed that cells with graphene oxide (η = 7.5%) performed better than those with the pure liquid electrolyte (η = 6.9%) due to an increase in the fill factor; however, no mechanistic rationale for improved performance was provided. Later work by Neo and Ouyang showed that graphene oxide can act as a gelator for methoxypropionitrile, a common low-volatility electrolyte solvent. They also report that the size of the graphene oxide sheets, which can be tuned by sonication time, is inversely related to the ionic conductivity of the gels.[183] DSSCs using well-ultrasonicated graphene oxide as the gelator were shown to retain relatively higher performance after a month of testing, although the nominal efficiency values were lower. Further details on the gelation process can be found in other works.[184,185] Even though device performance improvements were reported with gelation, with the emergence of tailored ionic liquids and solid-state hole conductors, gelation may become moot.

Table 3. Minimum Concentration of Graphene Oxide for Gelation at 23 °C for Solvents Containing 4 mM Tetramethylammonium Tetrafluoroborate[a]

solvent	minimum gelation concentration (wt % graphene oxide)
1-butanol	0.35
tetrahydrofuran	0.37
1-pentanol	0.4
acetonitrile	0.4
ethanol	0.57
water	0.8
diethylene glycol	1.4
dimethylformamide	1.5
dimethyl sulfoxide	1.6
benzene	not soluble
toluene	not soluble

[a]Data from Gun et al.[182]

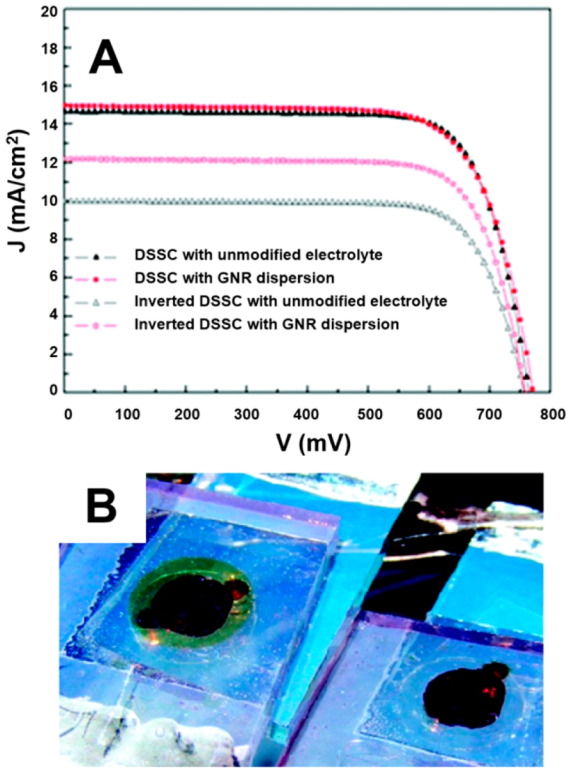

Figure 16. Photoinduced transparency of electrolyte with graphene nanoribbons. (A) *J*–*V* curves of front and back (inverted) illuminated DSSCs containing electrolytes with and without graphene nanoribbons (GNR). (B) Optical image of iodide/triiodide electrolyte without (left) and with (right) graphene nanoribbons under illumination. Adapted with permission from ref 180. Copyright 2011 American Chemical Society.

Shifting to high concentration, we first analyze the approach in general. The goal of using graphene materials as conductive fillers is to improve charge transport in the electrolyte. To conduct charge effectively, the graphene materials must be percolated throughout the electrolyte. Due to the large aspect ratio of the sheets, percolation has been reported to occur relatively early in composites (~0.05 wt % rheological percolation was reported for poly(methyl methacrylate)).[152] Yet, a percolated network which is in contact with both the anode and the cathode would create a short circuit in the device, diminishing performance. Furthermore, graphene sheets which would be effective for charge transport are too large to fit in the TiO_2 pores (which are ~10 nm), where much of the electrolyte resistance originates. Additionally, to be conductive the graphene materials must have a high degree of sp^2 hybridization; in other words, TRGO or graphene derived from liquid exfoliation or CVD would be preferred. These materials are also highly absorbing in the visible spectrum, preventing effective light transfer through a back illuminated

dx.doi.org/10.1021/cr400412a | *Chem. Rev.* XXXX, XXX, XXX–XXX

Table 4. Comparing DSSC Performance Parameters between Devices Using Graphene Materials as the Catalyst and Platinum Control Cells[a]

cathode	evidence	electrolyte	J_{SC} (mA/cm^2)	V_{OC} (V)	*FF*	η (%)	% change from Pt	ref
Pt nanoparticles		1 M DMPII, 0.1 M LiI, 0.12 M I_2, 0.5 M TBP in MPN	13.9	0.63	0.45	3.98		198
pyrenebutyrate-functionalized graphene			13.6	0.55	0.30	2.20	−45	
Pt nanoparticles		iodolyte AN-50, ACN solvent	12.8	0.70	0.68	6.02		199
TRGO (mild reduction)			10.6	0.68	0.22	1.60	−73	
CRGO (EPD)	R_{ct} > 75 000 Ω	iodolyte AN-50, ACN solvent	1.1	0.48	0.25	0.06		201
T-CRGO (EPD)	R_{ct} = 38 Ω		14.3	0.54	0.65	5.69		
sputtered Pt	R_{ct} not stated	0.6 M MPII, 0.5 M LiI, 0.05 M I_2, 0.5 M TBP in MPN	7.5	0.78	0.68	3.99		202
TRGO	R_{ct} = 22.3 Ω		5.9	0.65	0.56	2.13	−47	
Pt nanoparticles	**R_{ct} = 4.1 Ω cm^2**	0.65 M BMII, 0.03 M I_2, 0.5 M TBP, 0.05 M GSCN in 85% ACN/15% VN	12.8	0.83	0.68	**7.23**		203
T-CRGO (electrospraying)	**R_{ct} = 2.4 Ω cm^2**		12.2	0.81	0.70	**6.93**	−4	
Pt nanoparticles		0.6 M BMII, 0.1 M LiI, 0.03 M I_2, 0.5 M TBP, 0.1 M GSCN in 85% ACN/15% VN	16.2	0.67	0.60	6.44		204
graphene oxide (4 nm thick film)			9.6	0.50	0.09	0.50	−92	
TRGO (4 nm thick film)			16.4	0.66	0.33	3.60	−44	
Pt nanoparticles		0.5 M LiI, 0.05 M I_2, 0.6 M TBP in ACN	8.3	0.71	0.63	3.70		205
CRGO (vacuum filtration)			6.4	0.70	0.16	0.74	−80	
Pt nanoparticles	**R_{ct} = 2.0 Ω cm^2**	0.6 M MPII, 0.03 M I_2, 0.5 M TBP, 0.1 M GSCN in 85% ACN/15% VN	13.3	0.77	0.76	**7.76**		207
ultrasonic mixed T-CRGO	R_{ct} not stated		12.4	0.78	0.55	5.31	−32	
grinding mixed T-CRGO	**R_{ct} = 1.5 Ω cm^2**		12.8	0.78	0.72	**7.19**	−7	
Pt nanoparticles	R_{ct} = 0.4 Ω cm^2 at 0.75 V bias	iodolyte AN-50, ACN solvent	12.1	0.70	0.69	5.70		208
porous CVD-graphene	R_{ct} = 2.9 Ω cm^2 at 0.75 V bias		12.2	0.71	0.60	5.20	−9	
Pt nanoparticles	R_{ct} = 2.6 Ω cm^2	0.6 M DMPII, 0.1 M LiI, 0.05 M I_2, 0.5 M TBP (solvent unstated)	15.8	0.72	0.64	7.28		209
CRGO with SiO_2 spacers	R_{ct} + R_{pore} = 41 Ω cm^2		15.5	0.72	0.61	6.82	−6	
Pt nanoparticles	**R_{ct} = 8.8 Ω**	iodolyte AN-50, ACN solvent	14.3	0.79	0.66	**7.44**		211
N-doped TRGO film	R_{ct} not stated		11.8	0.73	0.49	4.20	−44	
N-doped TRGO foam	**R_{ct} = 5.6 Ω**		15.8	0.77	0.58	**7.07**	−5	
Pt on FTO	R_{ct} = 4.6 Ω	0.5 M MPII, 0.05 MI_2 in ACN	15.7	0.68	0.61	6.65		212
CVD-derived graphene	R_{ct} = 38 Ω		7.8	0.69	0.26	1.43	−78	
CVD-derived graphene, CF_4 functionalized	R_{ct} = 8.5 Ω		10.9	0.66	0.36	2.56	−62	
Pt nanoparticles	R_{ct} =1.1 Ω cm^2	0.6 M TBAI, 0.1 M LiI, 0.05 M I_2, 0.2 M TPB in ACN	13.4	0.74	0.68	6.79		23
porous TRGO with carbonaceous spacer	R_{ct} + R_{pore} = 0.9 Ω cm^2		13.4	0.74	0.69	6.79	0	
Pt nanoparticles	R_{ct} = 0.79 Ω cm^2; E_{pp} = 90 mV at 50 mV/s	iodolyte AN-50, ACN solvent	13.0	0.64	0.67	5.48		37
porous TRGO	R_{ct} = 9.4 Ω cm^2; E_{pp} = 150 mV at 50 mV/s		13.2	0.64	0.60	4.99	−9	
Pt nanoparticles	R_{ct} = 0.4 Ω cm^2	Z946: 1 M DMII, 0.15 M I_2, 0.5 M NBB, 0.1 M GSCN in MPN	13.1	0.71	0.74	6.89		38
GNP (85% transparent film)	R_{ct} = 308 Ω cm^2		13.1	0.72	0.52	5.00	−27	
Pt nanoparticles	R_{ct} = 0.76 Ω cm^2	1 M MPII, 0.05 M I_2, 0.5 M TBP, 0.5 M GSCN in ACN	18.5	0.71	0.58	7.59		39
porous T-CRGO	R_{ct} = 1.2 Ω cm^2		17.0	0.75	0.54	6.81	−10	
Pt nanoparticles	R_{ct} = 4.7 Ω cm^2	0.22 M $Co(L_1)_2(PF_6)_2$, 0.05 M $Co(L_1)_2(PF_6)_3$, 0.1 M $LiClO_4$, 0.2 M TBP in ACN	12.1	1.05	0.63	8.10		22
GNP (66% transparent film)	R_{ct} = 0.7 Ω cm^2		12.7	1.03	0.70	9.30	15	
Pt nanoparticles	R_{ct} = 5.5 Ω cm^2	0.22 M $Co(L_2)_3(PF_6)_2$, 0.05 M $Co(L_2)_2(PF_6)_3$, 0.1 M $LiClO_4$, 0.2 M TBP in ACN	14.0	0.90	0.65	8.20		216

dx.doi.org/10.1021/cr400412a | *Chem. Rev.* XXXX, XXX, XXX−XXX

Table 4. continued

cathode	evidence	electrolyte	J_{SC} (mA/cm^2)	V_{OC} (V)	*FF*	η (%)	% change from Pt	ref
GNP (66% transparent film)	R_{ct} = 0.08 Ω cm^2		14.8	0.88	0.72	9.40	15	
Pt nanoparticles	R_{ct} = 2.3 Ω cm^2	0.22 M $Co(L_2)_3(PF_6)_2$, 0.033 M $Co(L_2)_3(PF_6)_3$, 0.1 M $LiClO_4$, 0.2 M TBP in ACN	8.3	0.85	0.62	4.39		23
porous TRGO with carbonaceous spacer	R_{ct} + R_{pore} = 0.5 Ω cm^2		8.5	0.81	0.65	4.51	3	
Pt nanoparticles	R_{ct} = 55 Ω cm^2	0.1 mM dimethyldithiocarbamate, 0.1 M T_2, 0.5 M TBP in ACN	9.6	0.65	0.31	1.97		23
porous TRGO with carbonaceous spacer	R_{ct} + R_{pore} = 0.75 Ω cm^2		9.5	0.66	0.55	3.45	75	

[a]Fresh cell values used to be consistent. EIS assumed to be done at 0 V unless otherwise noted. ACN = acetonitrile; BMII = 1-butyl-3-methylimidazolium iodide; DMII = 1,3-dimethylimidazolium iodine; DMPII = 1,2-dimethyl-3-propylimidazolium iodide; EPD = electrophoretic deposition; GNP = graphene nanoplatelet, similar in properties to TRGO; GSCN = guanidinium thiocyanate: L_1 = 6-(1*H*-pyrazol-1-yl)-2,20-bipyridine; L_2 = 2,2′-bipyridine; MPII = L-methyl-3-propylimidazolium iodide; MPN = 3-methoxypropionitrile; NBB = *N*-butylbenzoimidazole; T_2 = 5-mercapto-1-methyltetrazole dimer; TBAI = tetrabutylammonium iodide; TBP = 4-*tert*-butylpyridine; VN = valeronitrile.

solar cell. Lastly, graphene materials have been shown to be catalytic toward DSSC redox mediators (see section 5 for details), with TRGO showing the highest activity. In this respect, pristine graphene (free of catalytic defects) or graphene oxide would be preferable. Even with these challenges several reports show improvements with this approach.

Ahmad et al. used high concentrations of solution-exfoliated graphene (up to 40 wt %) to create a gelled electrolyte containing an ionic liquid (1-methyl 3-propyl imidazolium iodide, PMII) with the goal of improving electrolyte conductivity.[36] Device performance was increased from η = 0.16% to η = 2.2% at 30 wt % loading of the graphene material; however, it is unclear to the authors of this review whether the improved performance over a PMII-only electrolyte device was due to either improved electrolyte conductivity or a shorter electrolyte diffusion length which could result from a percolation of the graphene material with the cathode, creating a structure similar to a porous carbon counter electrode (see section 5). In another approach to increase the conductivity of the electrolyte, Jung et al. used a lower concentration of graphene oxide (~6.5 wt %), which they solvothermally reduced in the electrolyte (1-octyl-2,3-dimethylimidazolium iodide, ODI, and iodide).[35] The device using this electrolyte performed better than one without the TRGO and even better than one based on acetonitrile (η = 5.8%, 3.6%, and 5.1%). Interestingly, an increase in electron lifetime was seen in the TRGO-containing DSSCs. We note that in both of the above studies, application of graphene material in the electrolyte may be severely limited by the catalytic activity of graphene for the reduction of triiodide, which could effectively create a short circuit in the cell.

Due to the high light absorption and catalytic activity of graphene materials, they are unlikely to be beneficial to high-performance DSSCs in high concentrations. Nevertheless, as a minor additive, such as to lower light absorption of the electrolyte, it is feasible that graphene materials are incorporated into the electrolytes of high-efficiency devices.

5. COUNTER ELECTRODE

For DSSCs which use redox mediators for charge transport, the reduced species regenerates the dye while the oxidized species is reduced at the cathode. For this system to work efficiently, (i) the redox species must be able to readily diffuse between the anode and the cathode, (ii) the rate of dye regeneration from the reduced species must be faster than from the semiconducting scaffold, and (iii) the rate of reduction of the redox species must be slow at the anode and fast at the cathode. Section 4 discusses ways which graphene materials have been used to address electrolyte diffusion limitations. Regarding (ii), TiO_2, and to a lesser extent FTO, is not highly active for reduction of the most common redox species (i.e., triiodide, $Co(bpy)_3$(III)). Although these slow kinetics are fortunate for the photoanode, they dictate that a catalyst material is required on the cathode to lessen the overpotential required to reduce to mediator species.

Cathodes composed of platinum nanoparticles deposited on FTO have been widely used due to their facile fabrication and high activity, particularly for the iodide/triiodide mediator.[6,7,186] There have been mixed reports on the stability of the precious metal in the DSSC system.[5,6,187] However, this concern has been rather moot for the research cells as they are often tested within 1 week of, if not the day of, fabrication. Furthermore, stability tests with Dyesol Platinum Paste PT1 have not shown a decrease in performance for the counter electrode over 11 000 h of testing.[188] Nevertheless, due to the undesirability of using an expensive metal such as platinum in a supposed low-cost DSSC and due to the high-temperature (~400 °C) fabrication methods required for traditional production of these electrodes, alternatives have been devised. Graphite and carbon black have been used as DSSC counter electrodes since at least 1996,[20] and in 2008 graphene materials were used for this role.[189] Between then and 2012 over 60 studies have been published looking at the effectiveness of using various graphene materials in the cathode, motivated by the material's high surface area, high conductivity, and tunability with respect to defects and composites. This section provides a comprehensive overview of these studies, first discussing the various techniques used to evaluate the effectiveness of the catalytic cathode. Second, we focus on studies using and modifying neat graphene materials and then look at studies which employ graphene materials in composites. As detailed below, either using high surface area networks of graphene materials or metal−[graphene material] composites can replace platinum with the iodide/triiodide redox mediator, while thin films of graphene materials are effective with other mediators such as $Co(bpy)_3$ (II/III). For reference, we include Tables 4 and 5 to compare device components and efficiencies for DSSCs using graphene material cathodes and their platinum control cells.

dx.doi.org/10.1021/cr400412a | *Chem. Rev.* XXXX, XXX, XXX−XXX

Table 5. Comparing DSSC Performance Parameters between Devices Using Graphene Material Containing Hybrids as the Catalyst and Platinum for Control Cells[a]

cathode	evidence	electrolyte	J_{SC} (mA/cm^2)	V_{OC} (V)	*FF*	η (%)	% change from Pt	ref
polymer hybrid								
Pt nanoparticles		iodolyte AN-50, ACN solvent	7.9	0.73	0.72	4.16		37
Vor-ink TRGO-based film			7.8	0.71	0.70	3.83	−8	
Pt		0.6 M DMPII, 0.1 M LiI, 0.05 M I_2, 0 3 M TBP in 80% ACN/20% THF	13.1	0.72	0.68	6.30		189
nanoparticles 1 wt % pyrenebutyrate-functionalized graphene, PSS/PEDOT			13.0	0.72	0.48	4.50	−29	
Pt	**R_{ct} = 90 Ω cm^2 at −0.6 V bias**; E_{pp} = 340 mV at 50 mV/s	0.6 M BMII, 0.03 M I_2, 0.5 M TBP, 0.1 M GSCN in 85% ACN/15% VN	9.4	0.77	0.70	**5.03**		210
N-doped CRGO, 10 wt % PVDF, 5 wt % CaB	**R_{ct} = 1.3 Ω cm^2 at −0.6 V bias**; E_{pp} = 581 mV at 50 mV/s		10.6	0.82	0.55	**4.75**	−6	
Pt	R_{ct} = 6.5 Ω cm^2	0.5 M LiI, 0.05 M I_2, 0 5 M TBP in 85% ACN/15% VN	9.1	0.67	0.55	3.37		221
TRGO with nation binder	R_{ct} = 11.7 Ω cm^2		7.7	0.68	0.54	2.82	−16	
Pt nanoparticles		not stated	12.4	0.77	0.70	6.68		223
HNO_2-doped CVD-derived graphene, PEDOT			12.8	0.77	0.63	6.26	−6	
Pt		0.3 M MPII, 0.3 M LiI, 0.05 M I_2, 0.3 M TBP in MPN	14.2	0.70	0.70	6.88		224
TRGO, polyanaline			13.3	0.69	0.67	6.09	−11	
Pt nanoparticles	**R_{ct} = 5.0 Ω cm^2, E_{pp} = 700 mV at 50 mV/s**	0.6 M DMPII, 0.1 M LiI, 0.05 M I_2, 0.5 M TBP in ACN	16.0	0.72	0.72	**8.34**		225
CRGO, polypyrrole	**R_{ct} = 1.1 Ω cm^2; E_{pp} = 520 mV at 50 mV/s**		15.8	0.73	0.71	**8.14**	−2	
Pt nanoparticles		0.6 M DMPII, 0.1 M LiI, 0.05 M I_2, 0.5 M TBP in ACN	9.4	0.74	0.66	4.50		226
TRGO, PDDA			9.1	0.71	0.47	3.10	−31	
TRGO			8.9	0.70	0.40	2.50	−44	
TRGO, PSS			8.7	0.69	0.35	2.10	−53	
CNT hybrid								
Pt	**R_{ct} = 569 Ω**	0.6 M MHII, 0.1 M LiI, 0.05 M I_2, 0.5 M TBP in MPN	14.6	0.69	0.73	**7.29**		214
TRGO paper (no substrate)	**R_{ct} = 3.4 Ω**		13.9	0.60	0.18	**1.50**	−79	
CNTs on TRGO paper	**R_{ct} = 0.7 Ω**		14.2	0.68	0.62	**6.05**	−17	
Pt nanoparticles	**R_{ct} = 1.7 Ω**	0.6 M MPII, 0.03 M I_2, 0.5 M TBP, 0.1 M GSCN in ACN	16.3	0.79	0.69	**8.80**		217
CRGO−CNT	**R_{ct} = 1.4 Ω**		16.1	0.75	0.63	**7.55**	−14	
Pt nanoparticles	R_{ct} = 8.2 Ω	1 M DMII, 0.05 LiI, 0.03 M I_2, 0.5 M TBP, 0.1 M GSCN in 85% ACN/15% VN	15.0	0.77	0.69	7.88		218
40% TRGO, 60% CNT (EPD)	R_{ct} = 9.8 Ω		12.9	0.78	0.61	6.17	−22	
evaporated Pt	**R_{ct} = 33 Ω cm^2**	0.6 M BMII, 0.03 M I_2, 0.5 M TBP, 0.1 M GSCN 85% in ACN/15% VN	10.3	0.72	0.70	**5.09**		219
60% T-CRGO, 25% CNT, 10 wt % PVDF, 5 wt % CB	**R_{ct} = 2.9 Ω cm^2**		11.4	0.77	0.53	**4.66**	−8	
metal hybrid								
sputtered Pt	R_{ct} = 7.7 Ω cm^2; I_p = 1.0 mA/cm^2	0.6 M MPII, 0 5 M LiI, 0.05 M I_2, 0.5 M TBP in ACN	5.1	0.68	0.59	2.00		91
TRGO, Ni nanoparticles	R_{ct} = 4.7 Ω cm^2; I_p = 1.2 mA/cm^2		5.2	0.70	0.60	2.19	10	
Pt nanoparticles	**R_{ct} = 11 Ω**	0.6 M DMPII, 0.1 M LiI, 0.05 M I_2, 0.5 M TBP in ACN	13.1	0.74	0.62	**6.08**		194
CRGO, $Ni_{12}Ps$ nanoparticles with carboxymethyl cellulose binder	**R_{ct} = 4.9 Ω**		12.9	0.73	0.61	**5.70**	−6	
Pt (PLD)	**R_{ct} = 6.2 Ω cm^2; I_p = 1.2 mA/cm^2**	0.6 M MPII, 0.5 M LiI, 0.05 I_2, 0.5 M TBP in ACN	5.8	0.69	0.53	**2.11**		215
TRGO, R (PLD)	**R_{ct} = 2.4 Ω cm^2; I_p = 1.6 mA/cm^2**		6.7	0.74	0.59	**2.91**	38	
sputtered Pt	**R_{ct} = 1.5 Ω cm^2**	0.6 M DMPII, 0.1 M LiI, 0.05 M I_2, 0.5 M TBP in ACN	15.3	0.71	0.75	**8.16**		227
T-CRGO, Pt nanoparticles (layer by layer EPD)	**R_{ct} = 1.3 Ω cm^2**		15.2	0.71	0.71	**7.66**	−6	

dx.doi.org/10.1021/cr400412a | *Chem. Rev.* XXXX, XXX, XXX−XXX

Table 5. continued

cathode	evidence	electrolyte	J_{SC} (mA/cm^2)	V_{OC} (V)	*FF*	η (%)	% change from Pt	ref
metal hybrid								
sputtered Pt (low temp)		E008: 0.1 M I_2, 1 M MPII, 0.5 M NMB, 0.1 M LiTFSI in MPN	13.1	0.72	0.67	6.29		228
coreduced GO, Pt nanoparticles			14.1	0.72	0.67	6.77	8	
evaporated Pt	R_{ct} = 33 Ω cm^2; **E_{pp} = 342 mV at 50 mV/s**	0.6 M BMII, 0.03 M I_2, 0.5 M TBP, 0.1 M GSCN in 85% ACN/15% VN	10.6	0.73	0.68	**5.27**		231
coreduced GO, Pt nanoparticles	R_{ct} = 0.67 Ω cm^2; **E_{pp} = 350 mV at 50 mV/s**		12.1	0.79	0.67	**6.35**	20	
sputtered Pt	**R_{ct} = 1.9 Ω cm^2**	1 M DMII, 0.15 M I_2, 0.5 M TBP, 0.1 M GSCN in MPN	13.4	0.72	0.66	**6.38**		235
TRGO, MoS_2 nanoparticles with 10 wt % PVDF, 10 wt % CaB	**R_{ct} = 0.57 Ω cm^2**		12.5	0.73	0.66	**6.04**	−5	

[a]Fresh cell values used to be consistent. EIS assumed to be done at 0 V unless otherwise noted. ACN = acetonitrile; BMII = 1-butyl-3-methylimidazolium iodide; CaB = carbon black; DMII = 1,3-dimethylimidazolium iodide; DMPII = 1,2-dimethyl-3-propylimidazolium iodide; EPD = electrophoretic deposition; GSCN = guanidinium thiocyanate; LiTFSI = lithium bis(trifluoromethanesulfonyl)imide; MPII = 1-methyl-3-propylimidazolium iodide; MPN = 3-methoxypropionitrile; NMB = *N*-methylbenzimidazole; PLD = pulsed laser deposition; TBP = 4-*tert*-butylpyidine; VN = valeronitrile.

5.1. Measurement Techniques

Here we briefly review some of the main measurement techniques used to qualitatively and quantitatively measure the effectiveness of a catalytic cathode. For full details, please see the referenced publications or an electrochemistry textbook, such as *Electrochemical Methods* by Bard and Faulkner.[190] Perhaps, the most convincing comparison of cathode performance is to fabricate DSSCs which only vary the cathode and then test photovoltaic characteristics (e.g., *I*−*V* curve, etc.) under standard solar conditions. However, this approach does not provide much insight into the catalytic activity of the electrodes themselves, and if one is looking to compare against a standard electrode such as platinized FTO, there is uncertainty as to the quality of the control cathode.

EIS, with an appropriate equivalent circuit, is useful in providing supporting evidence for a material's effectiveness in a DSSC. In particular, EIS can be used to determine R_{CT} for reduction of the redox species. EIS has been widely used to study the reduction of triiodide on platinum electrodes, and a robust equivalent circuit has been developed for a symmetrical sandwich cell electrode setup (see Figure 17) using electrolytes

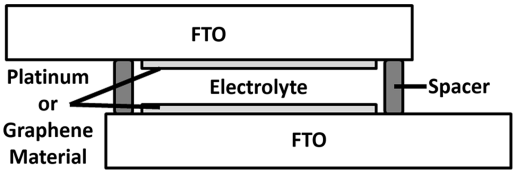

Figure 17. Sandwich cell configuration schematic for EIS testing.

found in DSSCs.[6,7] For 5−10 μg/cm^2 platinum loading of thermalized chloroplatinic acid, R_{CT} can be expected to be around 1 Ω cm^2 at zero applied bias.[6,191] For high-performance DSSCs, this results in a voltage drop of 10−20 mV, about a 2% relative loss from an ideal interface. Applying a bias can significantly lower the obtained R_{CT} values, due to an increased reaction rate as suggested by Butler−Volmer kinetics.[6] Thus, although R_{CT} values obtained from EIS measurements at an applied bias are sometimes reported, these are not valid comparisons to most literature results or to predict how the electrode would behave in a DSSC where one wants to operate close to zero overpotential.

The EIS equivalent circuit confirmed for platinum electrodes (Figure 18A) has been used for many flat, conductive electrodes. However, for porous, high surface area electrodes, Roy-Mayhew et al. proposed an equivalent circuit which accounts for diffusion in the pores (Figure 18B).[37] For these systems (i.e., porous TRGO (i.e., FGS) films) high-, mid-, and low-frequency phenomena are ascribed to diffusion resistance in the pores (N_{pore}), catalytic charge transfer resistance (R_{CT}), and bulk diffusion (N_{bulk}), respectively. However, often in carbonaceous systems R_{CT} and N_{bulk} overlap, making it difficult to identify and quantify the appropriate effects. In these cases, a bias can be applied to the cell, wherein R_{CT} should decrease and N_{bulk} should increase. An alternative equivalent circuit, which can explain similar features on a Nyquist plot, was postulated by the S.-W. Rhee group.[192,193] This model assumes that the high-frequency semicircle is due to charge transport through the carbon film (R_{trns}, C_{trap}) and that the mid- and low-frequency semicircles are due to catalysis (R_{ct}) and diffusion (Z_N), respectively. A third alternative equivalent circuit used is based on the assumption that the midfrequency semicircle is due to an adsorption event (Z_{w1}), with the high- and low-frequency semicircles arising due to catalysis (R_{ct}) and diffusion (Z_{w1}), respectively.[194,195] Note that while the traditional platinum equivalent circuit and that suggested by Roy-Mayhew et al. (Figure 17A and 17B) are used with symmetrical cells to back out the resistance of a single electrode (hence the $2R_{CT}$), the other two models are for a single electrode (Figure 18D and 18E). While we do not prescribe a correct model in this review, we do note that having an inaccurate one can easily lead to erroneous results and could explain inconsistencies with R_{CT} and DSSC performance data, such as those seen in Tables 4 and 5 (highlighted in bold text).

In addition to EIS, cyclic voltammetry (CV) is commonly used for evaluating catalyst effectiveness. In this case, a dilute electrolyte is used (for iodide/triiodide systems this is usually ∼5 mM LiI, 0.5 mM I_2, and 0.1 M $LiClO_4$ in acetonitrile) to ensure that diffusion becomes limited. An appropriate reference electrode (e.g., nonaqueous, Ag/Ag^+ for the case of acetonitrile-based electrolyte) helps ensure reliability of measurements. From the CV, two values are often cited as evidence for activity: peak-to-peak separation, E_{pp}, and peak current, I_p, and these are compared with a platinum control electrode. We note that high

dx.doi.org/10.1021/cr400412a | *Chem. Rev.* XXXX, XXX, XXX−XXX

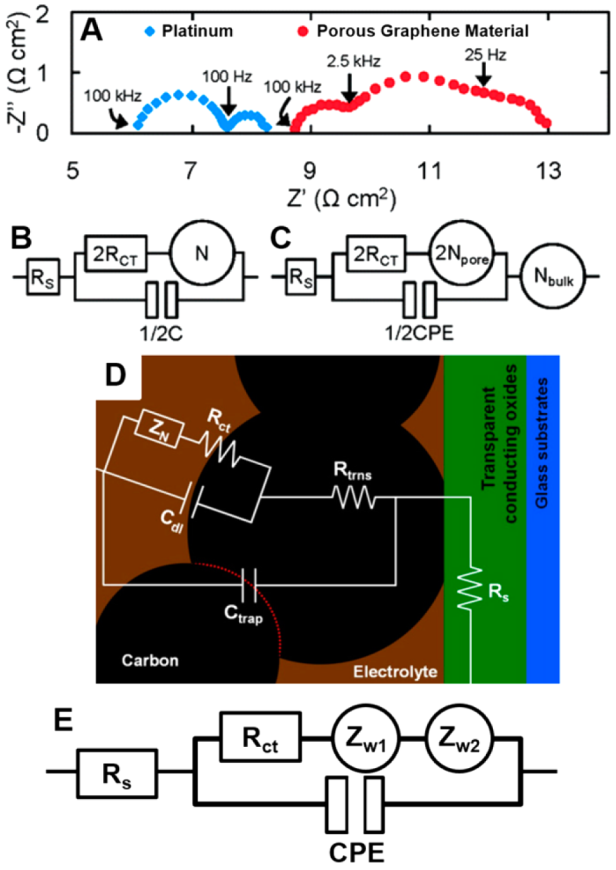

Figure 18. EIS analysis methods. (A) Sample EIS Nyquist plot showing the two semicircles characteristic of platinum electrodes and three features characteristic in some graphene material electrodes. These spectra were taken at 0.5 V bias to accentuate the observance of the three features with the graphene material (TRGO). (B) Traditional equivalent circuit for platinum electrodes in a sandwich cell testing setup. (C) Equivalent circuit proposed by Roy-Mayhew et al. accounting for porosity in the high surface area graphene material electrodes. (A, B, and C) Adapted with permission from ref 37. Copyright 2010 American Chemical Society. (D) Proposed equivalent circuit with carbon black electrodes accounting for resistance in the electrode. Reprinted from *Electrochim. Acta*, ref 193, Copyright 2012, with permission from Elsevier. (E) Proposed equivalent circuit looking to incorporate adsorption as described in Dou et al.[194]

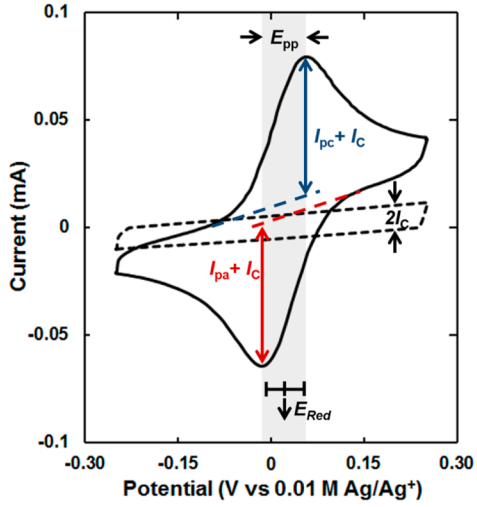

Figure 19. Interpreting a cyclic voltammogram. Curves are for an electrode made of platinum nanoparticles on a conductive substrate with electrolytes containing cobalt–bipyridine redox mediator with a supporting electrolyte (solid line) and containing supporting electrolyte only (dashed line). Dashed line represents the capacitive charging, and the width is equal to twice I_C. With high surface area electrodes, peak currents cannot be measured directly from the plots; rather the contribution of the anodic or cathodic current (represented by colored dashed lines) and I_C must be taken into account. E_{pp} is the difference between the potential of the cathodic and anodic peaks as represented by the thickness of the gray band. E_{Red} is the potential value midway between the two peaks. Reprinted with permission from ref 2. Copyright 2013 Joseph Roy-Mayhew.

surface area platinum particles are generally used in DSSCs, so a similar control should be used in electrochemical measurements. Polished platinum plate electrodes will provide a false control with lower activity than what platinum nanoparticles achieve in devices. In general, the smaller the E_{pp} the faster the reaction and more catalytic the surface; however, we would like to note that this may be due to morphology rather than to the intrinsic activity of the material.[196,197] I_p can also be a measure of activity; however, it is important to account for any capacitive background current (I_C) and any diffusion-limited current from secondary reactions (in the case of multiple electron systems such as with iodide/triiodide). If the absolute value of the peak is reported, as is sometimes done, the value will be inflated from those contributions to current, which are not caused by the catalytic activity of the material. A sample cyclic voltammogram for a one-electron reaction, $Co(bpy)_3$(II/III), with parameters of interest, is shown as Figure 19. Less often used to compare counter electrode catalytic activities are Tafel curves, which can also be extracted from CV or linear sweep potentiometry. In these plots of the logarithm of current versus overpotential there is a linear region where the back reaction is negligible and mass transfer is not limiting. This region can be extrapolated to zero overpotential to determine the exchange current and from this R_{CT}.

5.2. Graphene Materials

The first study incorporating graphene materials as the catalytic cathode of a DSSC that we are aware of was by Xu et al., where pyrenebutyrate was used to stabilize CRGO suspensions for processing into a film.[198] Although the film worked better as a cathode in a DSSC (η = 2.2%) than bare FTO did (η = 0.05%), it was obvious that many improvements would have to be made to be able to compete with the conventional platinized FTO (η = 4.0%). Choi et al. found similar performance limitations using graphene oxide films which had undergone mild thermal treatment (250 °C, 2 min in air) (see Table 5).[199] Hasin et al. compared TRGO and CRGO films and found that the former exhibit about one-fourth of the R_{CT} of the latter.[200] Nevertheless, this resistance was still over 70 times greater than that of platinized FTO ($R_{CT} \approx$ 180, 48, and 0.66 Ω cm^2 for CRGO, TRGO, and platinized FTO electrodes). Although not focused on in their work, this result could be indicative that defect sites—created through thermal reduction—could be catalytic for the triiodide reduction. Roy-Mayhew et al. looked to improve upon these results by utilizing a porous network of TRGO formed through spin coating a polymer–TRGO composite and thermalizing the polymer binder.[37] This work showed that TRGO films could be a viable competitor for platinum (TRGO R_{CT} = 9.4 Ω cm^2, η = 5.0%; platinized FTO R_{CT} = 1.3 Ω cm^2, η = 5.5%) and suggested that the functional groups and defects could play an important role in catalysis.

dx.doi.org/10.1021/cr400412a | *Chem. Rev.* XXXX, XXX, XXX–XXX

Since then a series of studies has been published analyzing how the degree of reduction affects catalytic performance.[30,39,201−204] Zhang et al. found that thermal annealing of porous CRGO films increased activity up to 400 °C in air, above which activity decreased.[39] The reported R_{CT} for the T-CRGO film at 400 °C was ∼280 times lower than that for electrodes heated only to 250 °C—the lowest used in the study and similar to the treatment reported for Choi et al. above. Unlike the T-CRGO films used by Zhang et al., a separate study by Choi et al. showed a monotonic decrease in R_{CT} for CRGO thermally treated at progressively higher temperatures—up to 600 °C, the maximum used in their study.[201] Hsieh et al. also report a monotonic increase in performance with an increase in reduction temperature of graphene oxide, with films (20 μm thick with 5% polyvinylidene fluorine, PVDF) annealed at 700 °C exhibiting an R_{CT} of 22 Ω cm^2.[202] Nevertheless, device efficiency was only slightly over one-half that of cells using sputtered platinum. Jang et al. report an increase in activity upon thermal treatment of 200 nm thick electrosprayed CRGO films and believe it is due to an increase in network conductivity (by a factor of ∼40) rather than to the intrinsic activity of the material.[203] They follow this work up with a systematic study of thermal annealing of flat films of graphene oxide (∼4 nm thick).[204] Morphology is minimized in this system, so the changes seen are due to the material rather than the structure. Detailed electrochemical studies were not undertaken; nevertheless, the authors show a strong increase in performance with increased temperature treatment (η = 0.50%, 0.51%, 2.9%, and 3.6% for graphene oxide and graphene oxide thermally reduced at 150, 250, and 350 °C, respectively). Although impressive improvement was seen, the best cells only exhibit a fill factor of 0.33 and are significantly worse than the platinized FTO electrode (n = 6.4%), reinforcing the relative inertness of the carbon material for the iodide-based redox mediator.

As introduced above, two main approaches to overcome the limitation of a relatively inert material have been taken: (i) improving morphology, generally by increasing the surface area and pore size,[23,37,205−209] and (ii) increasing the intrinsic activity of the material through chemical modification.[210−213] With the first approach, a straightforward technique is to use more material and make a thicker film; however, simple liquid-processing techniques such as vacuum filtration do not produce films which can compete with platinum.[205] Wu and Zheng created horizontal oriented CRGO using spin coating and vertically oriented CRGO using electrophoretic deposition.[206] In their system they showed that the vertical orientation had greater activity, suggesting that ion mobility and assessable surface area was higher in this system. However, the deposition procedure used $NiCl_2$, so we cannot rule out that the improved performance was due to the 1 wt % of Ni that was deposited during the process. In another study, Zheng et al. showed that grinding CRGO in poly(ethylene glycol) and then thermolyzing the polymer led to films with larger pores (by ∼1 nm) and DSSCs with higher efficiencies (η = 7.2%) than those created from ultrasonicating CRGO in the polymer (η = 5.2%).[207] Even so, these devices still did not match the performance of those using platinized FTO (η = 7.8%). To create high surface area electrodes, Lee et al. first created a $NiCl_2$−poly(vinyl alcohol) film and then pyrolyzed it to form a porous nickel substrate.[208] Through CVD processing and subsequent etching of the metal scaffold, a porous (average pore size 40−50 nm) CVD-derived graphene structure was formed. Another approach was to use spacers to keep RGO sheets apart and thus increase the surface area. Gong et al. used 12 nm SiO_2 particles as spacers to increase their CRGO film specific surface area from 8.6 to 383.4 m^2/g.[209] Even with the improvement, platinized FTO performed 6% better, relatively, than the film with spacers. Roy-Mayhew et al. were able to match the performance of platinized FTO (η = 6.8% for both) by doctor blading a TRGO (Vor-x, Vorbeck Materials Corp.) film with an ethyl cellulose binder and then partially thermalizing the binder, leaving behind an insoluble residue that prevented TRGO sheets from restacking.[23]

Rather than focusing on increasing the surface area, several groups worked on increasing the intrinsic activity of the material through chemically doping the material.[210−213] Yen et al. over doubled the efficiency of their CRGO−PVDF−[carbon black] films (from η = 1.9% to η = 4.8%) by incorporating nitrogen into them through hydrazine reduction in the presence of ammonia.[210] Similarly, Xue et al. created nitrogen-doped graphene through annealing graphene oxide in an argon and ammonia atmosphere, and this material outperformed traditional TRGO in a DSSC, reportedly due to an increase both in catalytic structural defect density and in conductivity.[211] Nevertheless, in the same study, better performance was seen with high surface area nitrogen-doped graphene created through annealing freeze-dried graphene oxide. Images of these electrodes are shown in Figure 20A and 20C. They formed counter electrodes from this material by mixing it with poly(ethylene oxide), coating FTO, and thermalizing the binder. The authors report lower R_{CT} than platinum with these films; however, in contradiction to these results, DSSCs using platinized FTO were reported to have slightly higher efficiencies (η = 7.4% compared to η = 7.1%). Table 5 lists device performances for the articles reviewed. As mentioned previously, where there is a discrepancy between EIS or CV results and η, such as that just described; the results are highlighted in bold font.

Other methods to improve the intrinsic activity of graphene materials include CF_4 functionalization[212] and HNO_3 treatment.[213] As mentioned in section 3.1, HNO_3 treatment has been shown to decrease to resistance of large-area CVD−graphene films. In addition to this effect, Das et al. demonstrate a decrease in R_{CT} from 45 to 7.9 Ω cm^2 on CVD-derived graphene with a treatment of 70% HNO_3, a result which could be due to a shift in the Fermi level of the film from 4.52 to 5.21 eV.[213] Treatment with 100% HNO_3 resulted in a film with greater R_{CT} (19.3 Ω cm^2) and Fermi level (5.31 eV). These benefits may not be as significant as they appear in this study, as the group has been able to achieve an R_{CT} of 16.3 Ω cm^2 for CVD-derived graphene using the same electrolyte.

Interestingly, a third approach taken by Kavan et al. has also proven successful in fabricating high-performing DSSC cathodes, namely, changing the electrolyte system.[38] In their work, Kavan et al. deposit thin layers of commercial graphene nanoplatelets (few-layered graphite, GNP, Cheap Tubes Inc.) through drop-casting dilute suspensions. This process resulted in highly transparent films on FTO. Using an ionic liquid electrolyte R_{CT} was decreased 5−6 times lower than using a solvent (methoxypropionitrile) based system, which is the opposite of what would be expected based on viscosity.[6] Using cathodes with T > 85%, DSSCs were able to achieve η = 5%, compared to η = 6.89% of those cells using platinized FTO.

All of the heretofore mentioned devices were based on the iodide/triiodide redox couple. However, even more promising

dx.doi.org/10.1021/cr400412a | Chem. Rev. XXXX, XXX, XXX−XXX

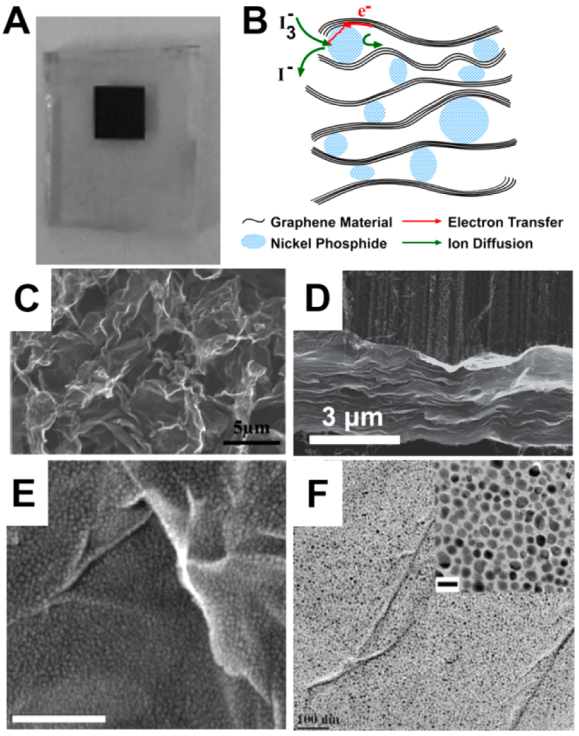

Figure 20. Graphene material electrodes for catalysis. (A) Optical image of a typical opaque graphene material electrode. Adapted with permission from ref 211. Copyright 2012 John Wiley & Sons. (B) Schematic of the use of graphene materials as conductive scaffolds for high-activity materials. Similar depiction to that in Dou et al.[194] (C) SEM image of porous nitrogen-doped graphene film, as shown in A. Adapted with permission from ref 211. Copyright 2012 John Wiley & Sons. (D) SEM image of CNT-TRGO hybrid electrode wherein TRGO acts as a conductive base for vertically aligned CNTs. Adapted with permission from ref 214. Copyright 2011 John Wiley & Sons. (E) SEM image and (F) TEM image of nickel nanoparticles deposited on TRGO. Scale bar for E is 100 nm. Inset scale bar for F is 10 nm. Adapted with permission from ref 215. Copyright 2011 American Chemical Society.

results were seen with cobalt-based and sulfur-based mediators.[22,23,157] For instance, graphene nanoplatelet films similar to those prepared in the previous study by Kavan et al. outperform platinized FTO with both the $Co(bpy)_3$(II/III) and the $Co(L)_2$ redox couples, where L is 6-(1*H*-pyrazol-1-yl)-bpy.[22,216] DSSCs fabricated using these electrolytes and 66% transparent graphene nanoplatelet cathodes exhibited efficiencies over 9%, and with the latter electrolyte a V_{OC} greater than 1 V was achieved. These devices exhibit 12% and 15% greater relative efficiencies, respectively, than those DSSCs using platinized FTO cathodes. At 97% transparency, approximately a monolayer of graphene coverage on average, the R_{CT} for the $Co(bpy)_3$ redox couple was 4.3 Ω cm^2. It is suggested that these nanoplatelets are so catalytic for the $Co(bpy)_3$ mediator that the redox couple could be used as a sensor to determine if any platelets were present even at negligible visible absorption. Roy-Mayhew et al. saw similar results for their porous TRGO electrode with the $Co(bpy)_3$ redox couple (η = 4.5% with TRGO, η = 4.4% with platinized FTO) and saw an even sharper contrast with the platinized FTO for the sulfur system (η = 3.5% and 2.0%) as expected due to platinum's poor activity with the sulfur system.[23]

5.3. Hybrid Electrodes

Although it has been demonstrated that graphene materials, depending on their processing, can compete directly with platinum, many researchers have found working with graphene material composites to be more fruitful, with the idea that graphene materials can be a conductive scaffold for highly catalytic particles (e.g., Figure 20B). An intuitive pairing has been with graphene's 1-D counterpart, CNTs. Li et al. used TRGO papers and vertically aligned CNTs grown on these papers as standalone cathodes (i.e., no conductive substrate).[214] These films (Figure 20D) were about 3 μm thick and had an R_{Sh} of 50 Ω/sq, about 4 times greater than that of FTO typically used. In a DSSC, TRGO paper performed poorly (η = 1.5%); however, addition of the CNTs drastically improved performance (η = 6.05%) to 83% that exhibited by DSSCs using platinum cathodes (η = 7.3%, form of platinum electrode unstated). Similarly, Velten et al. showed that a composite CNT−CRGO hybrid film had lower R_{Sh} and R_{CT} (15 Ω/sq, 1.4 Ω) than CRGO (94 Ω/sq, 20 Ω) or CNT films (30 Ω/sq, 4.3 Ω) alone and corresponding performance was seen in DSSCs as well.[217] Zhu et al. used electrophoretic deposition to codeposit CNTs and RGO (microwave-assisted reduction).[218] They saw a peak performance at 60% CNT, 40% RGO.[219] This result was similar to that from a study by Chang et al., which found their best loading to be 70% CNT, 30% CRGO. Yet, not all studies showed benefits in the hybrid electrode. Kim et al., also using electrophoretic deposition formed films, found that TRGO films were superior to both CNT films and TRGO−CNT hybrid films.[220] The contrast in these results is not known but could be due to different processing of the carbon materials resulting in materials with fewer (or more) active sites (i.e., defects or functional groups).

Hybrids of graphene materials and polymers have been studied for a variety of improved characteristics including durability, adhesion, conductivity, and catalytic activity. TRGO films with Nafion and polyvinylpyrrolidone binders have been employed;[221,222] however, they run into the same catalytic limitations of low-porosity TRGO films. HNO_3-doped CVD-derived graphene (4 layers) were used as a conductive substrate for ∼110 nm poly(3,4-ethylenedioxythiophene) (PEDOT) films.[223] RGO has also been used as a scaffold for polymer nucleation as detailed by Wang et al. for polyanaline[224] and Gong et al. for polypyrrole.[225] Hong et al. used 1 wt % CRGO as a conductive and catalytic filler in 60 nm thick poly(styrenesulfonate) (PSS):PEDOT films.[189] However, this performance might have been diminished due to charge repulsion between negatively charged polymer and negatively charged triiodide. Corroborating this idea, Kaniyoor and Ramaprabhu found that a cationic polyelectrolyte (polydiallyldimethylammonium chloride) improved the performance of TRGO, while an anionic polyelectrolyte (PSS) diminished it.[226] Nevertheless, as can be seen in Table 5, no polymer−[graphene material] hybrid has been able to match the performance of platinum cathodes for the iodide/triiodide mediator.

To match or exceed the performance of platinized FTO electrodes, several groups developed platinum−RGO hybrid electrodes.[227−231] Gong et al. found that using a layer of CRGO as an intermediate layer between FTO and platinum they could reduce the platinum loading to ∼0.2 μg/cm^2, with performance close to that of sputtered platinum (η = 7.7−8.2% for platinum).[227] Using photoassisted coreduction of chloroplatinic acid and graphene oxide, Tjoa et al. was able to form 3 nm particles on RGO, which when sprayed onto FTO (1 μm thick)

dx.doi.org/10.1021/cr400412a | *Chem. Rev.* XXXX, XXX, XXX−XXX

outperformed platinum films formed from low-temperature sputtering.[228] In this case, the activity of the platinum control (as evidenced by R_{CT}) was not reported. Li et al., in an alternate approach, coreduced graphene oxide and chloroplatinic acid with microwaves.[229] In their study, Chartarrayawadee et al. showed that it was preferable to codeposit CRGO and platinum rather than subsequently, layer by layer, which would follow from graphene sheets forming low-permeability films inhibiting diffusion to the underlying active platinum particles.[230] Nanoparticles with more common metals were deposited on RGO as well, including $Ni_{12}P_5$ and MoS_2 among others.[91,194,232−235] Bajpai et al. deposited ∼8 nm diameter Ni particles on TRGO by laser ablation, resulting in a cathode which outperformed sputtered platinum (SEM and TEM images are shown in Figure 20E and 20F),[91] and Das et al. improved the activity of CVD-derived graphene by depositing 30−50 nm CoS particles through a successive ionic layer absorption and reaction (SILAR) method.[232] Furthermore, in their record efficiency quantum dot solar cell (5.4%), Santra and Kamat utilize a Cu_2S−RGO hybrid counter electrode[236] which the research group had previously explored.[233]

Many studies have tried to match the performance of platinum as a catalyst using graphene materials, but few have succeeded (see Figure 21). TRGO, formed at higher temperatures, is more promising than CRGO or pristine graphene; however, with the iodide/triiodide redox couple, large area networks of graphene materials are required. Although thick layers of materials can work for this role, electrodes can become limited by diffusion through the porous network and resulting films are opaque. With the cobalt- and sulfur-based mediators, any type of graphene material may be sufficient, though again less material will likely be required for TRGO material. Catalysis of these materials is likely aided by the defect sites and edges present in these materials. For the iodide/triiodide redox couple, efficient thin transparent layers are likely only with hybrid materials, and for this, TRGO may be the most promising due to its strong stabilization of nanoparticles at defect sites.[111]

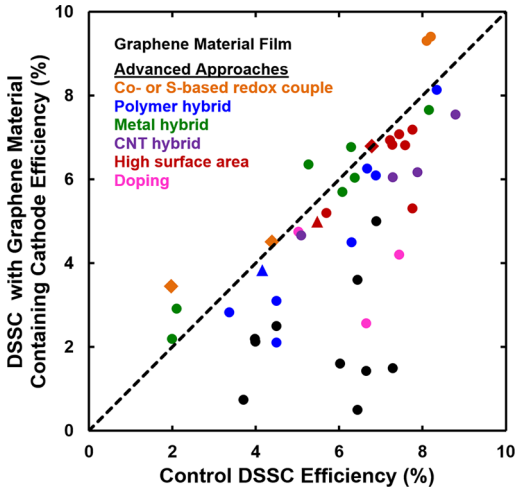

Figure 21. Comparison of reported efficiencies for DSSCs with and without graphene materials as the cathode catalyst. Colors correspond to the general approach. (Black) Basic use of graphene materials as the catalyst. (Blue) Polymer−[graphene material hybrid]. (Green) Metal−[graphene material] hybrid. (Orange) Graphene material electrodes with cobalt- or sulfur-based redox couples. (Pink) Electrically doped graphene material electrodes. (Red) High surface area graphene material structures. Reprinted with permission from ref 2. Copyright 2013 Joseph Roy-Mayhew.

6. GRAPHENE APPLICATIONS IN OTHER TYPES OF SOLAR CELLS

For many of the same reasons that they have been used in DSSCs, graphene materials have also been used in other types of solar cells. A brief overview is included here to provide context for the DSSC work. As mentioned in section 3.1, transparent conductors are a large potential market, and having cost-effective TCFs would allow improvements to conventional silicon solar cell technologies as well as to the thin film technologies (cadmium telluride, copper indium gallium selenide, organic, etc.), allowing for device structure modification, and a reduction in the number of silver contact lines on devices. Along these lines, a graphene material-based conductive ink could displace silver current collectors in the gamut of solar cell technologies. Currently, it is estimated that silver contact lines represent about $0.04/$W_P$ of devices and is highly dependent on the cost of silver.[237] Furthermore, most silver pastes currently marketed have to be sintered at elevated temperatures (>400 °C), increasing processing costs and limiting substrate selection. To be applicable, any replacement inks would have to achieve similar conductivity, both along the busbars and in contacting the device TCF without shading more of the device, a daunting task. In organic solar cells, graphene materials have been used as electron acceptors[238] and hole conductors, which a few reviews summarize.[239−241] Additionally, graphene materials have been used to form Schottky junctions with CdSe[242] and Si[243,244] with the later device achieving η > 8%. In line with this work, researchers have used graphene dispersions to facilitate stable growth of attached nanoparticles for quantum dot solar cells and for solar fuel applications.[245−247] Lastly, fundamental studies of graphene have shown hot carrier transport[248,249] and multiple carrier generation from a single photon,[172] both effects which overcome the limits imposed on devices based on the band gap of semiconductors, and thus, a graphene photovoltaic device could obtain very high efficiencies in the future. Graphene materials have been used with a range of solar cell technologies, but what is distinguishing about DSSCs is that graphene materials, with their wide range of properties, have been used in almost all aspects of the device.

7. CONCLUSIONS AND OUTLOOK

Although graphene materials can be used to improve DSSCs in a variety of roles, particular functions are best performed by specific graphene materials. Pristine graphene, followed by highly reduced graphene oxide, have the best prospects for transparent conductors, though by themselves the materials are not sufficient to meet application demands. These materials will have to either be electronically doped or exist as a part of a metal hybrid system. In the photoanode, graphene materials have resulted in improved photocurrent; however, it is unclear whether the advantages will apply to optimized devices. Whether graphene oxide, CRGO, or TRGO is processed with the TiO_2 is unlikely to mater significantly, as heat treatment is generally required to sinter the TiO_2 layer, which will thermally reduce the graphene material. If there is a percolated graphene material network then sintering may not be necessary; however, each TiO_2 particle would have to be in contact with the

dx.doi.org/10.1021/cr400412a | Chem. Rev. XXXX, XXX, XXX−XXX

graphene material network for best results. In this case, the sheets would have to be conducting and well dispersed through the TiO_2 matrix, so starting processing with graphene oxide and then reducing the material is a promising option. Pristine graphene could be advantageous in this application due to its high conductivity and relative inertness, but processing would be difficult, limiting application. Graphene materials can be used as a sensitizer in solar cells, and quantum effects, in particular, hot injection, could allow cells to exceed the Shockley–Queisser efficiency limit. Nevertheless, optimization processing of graphene quantum dots has brought the material closer to current organic dye structures. Graphene oxide could be a useful gelling agent in the electrolyte, whereas RGO in this role will likely catalyze recombination and reduce cell efficiency. At the cathode, two approaches have been shown that can equal or surpass the performance of platinum nanoparticles: (i) high surface area electrodes and (ii) high-activity materials. In both approaches RGO is advantageous as pristine graphene is relatively inert. In the first case, care must be taken to prevent restacking of sheets, while in the second, either a highly active nanoparticle composite can be formed or a redox mediator for which reduced graphene oxide is highly active (e.g., $Co(bpy)_3$(II/III)) can be used. Use of graphene materials in DSSCs has seen a rapid increase in research and fruitful results. Nevertheless, as research progresses, it is important to keep in mind that the various graphene materials have different properties—integrally tied to their method of production—and each may be beneficial to different areas in a solar cell. A next stage of research, to bring graphene materials to higher relevance in the DSSC community, would be to study whether improvements discussed within this review can be carried over to the current best-in-class devices.

AUTHOR INFORMATION

Corresponding Author

*E-mail: iaksay@princeton.edu.

Notes

The authors declare no competing financial interest.

Biographies

Joseph Roy-Mayhew received his B.S. degree from the Massachussets Institute of Technology and Ph.D. degree in Chemical Engineering from Princeton Unversity. His research focuses have been on advanced materials in energy technologies as well as the interplay of energy technology and environmental policy. In 2012, he spent time as a visiting researcher at Uppsala University with Anders Hagfelt and Gerrit Borschloo. He is currently working to commercialize graphene-enabled technologies at Vorbeck Materials Corp. in Jessup, MD.

Ilhan Aksay is a Professor in the Department of Chemical and Biological Engineering of Princeton University. He earned his B.Sc. (1967) degree in ceramic engineering at the University of Washington, Seattle and his M.Sc. (1969) and Ph.D. (1973) degrees in Materials Science and Engineering at the University of California, Berkeley. Prior to joining Princeton in 1992, his teaching and research affiliations included appointments at the University of Washington, Seattle (1983–92), University of California, Los Angeles (1981–83), the Middle East Technical University, Ankara, Turkey (1975–81), and Xerox Corporation, Webster Research Center, Webster, NY (1973–75). His research activities include the processing science of ceramic matrix composites, thermodynamics and phase equilibria in materials systems, diffusion and structural studies in ionic systems, interfacial reactions and capillarity phenomena, and utilization of self-assembly techniques in materials processing. His most recent work on *functionalized* graphene produced through thermal reduction of graphene oxide demonstrated many advantages in technologies ranging from nanocomposites to electrochemical devices for chemical sensing, energy harvesting, and energy storage. He received the Richard M. Fulrath (1987) and the Edward C. Henry (2000) Awards of the American Ceramic Society, the Charles M. A. Stine Award of the American Institute of Chemical Engineers (1997), and the Turkish National Medal of Science (Tübitak) (2001). He is a member of the U.S. National Academy of Engineering, NAE (2010), and the Science Academy, Turkey (2012). In recognition of his research and efforts in promoting technology transfer, he was named the Puget Sound (Washington State) Engineering Council's 1988 Academic Engineer of the Year. He is a Fellow of the American Association for the Advancement of Science (AAAS) and the American Ceramic Society and an honorary member of the Japanese Materials Research Society.

ACKNOWLEDGMENTS

The authors thank A. Hagfeldt, G. Boschloo, N. Vlachopoulos, E. Unger, and K. Nonomura of Uppsala University as well as C. Punckt and M. Pope of Princeton University for helpful discussions on dye-sensitized solar cells and electrochemistry. Dye-sensitized solar cell schematics were created by I. Ocko with support from the Princeton Environmental Institute.

ABBREVIATIONS

ACN	acetonitrile
BMII	1-butyl-3-methylimidazolium iodide
bpy	bipyridine
C/O	atomic carbon to oxygen ratio
CB	conduction band
CaB	carbon black
CNT	carbon nanotube
CRGO	chemically reduced graphene oxide

dx.doi.org/10.1021/cr400412a | *Chem. Rev.* XXXX, XXX, XXX–XXX

CVD	chemical vapor deposition
DMII	1,3-dimethylimidazolium iodine
DMPII	1,2-dimethyl-3-propylimidazolium iodide
DSSC	dye-sensitized solar cell
EIS	electrochemical impedance spectroscopy
EPD	electrophoretic deposition
FGS	functionalized graphene sheet
FTO	fluorine-doped tin oxide
GNP	graphene nanoplatelet
GNR	graphene nanoribbon
GSCN	guanidinium thiocyanate
GQD	graphene quantum dot
HOMO	highest occupied molecular orbital
ITO	indium tin oxide
LiTFSI	lithium bis(trifluoromethanesulfonyl)imide
LUMO	lowest unoccupied molecular orbital
MPII	1-methyl-3-propylimidazolium iodide
MPN	3-methoxypropionitrile
NBB	*N*-butylbenzoimidazole
NMB	*N*-methylbenzimidazole
ODI	1-octyl-2,3-dimethylimidazolium iodide
PEDOT	poly(3,4-ethylenedioxythiophene
PMII	1-methyl 3-propyl imidazolium iodide
PSS	poly(styrenesulfonate)
PVDF	polyvinylidene difluoride
RGO	reduced graphene oxide
SEM	scanning electron microscopy
SILAR	successive ionic layer absorption and reaction
TBAI	tetrabutylammonium iodide
TBP	4-*tert*-butylpyridine
TCF	transparent conducting film
T-CRGO	thermally treated chemically reduced graphene oxide
TEM	transmission electron microscopy
TRGO	thermally reduced graphene oxide
VB	valence band
VN	valeronitrile

REFERENCES

(1) O'Regan, B.; Grätzel, M. *Nature* **1991**, *353*, 737.
(2) Roy-Mayhew, J. D. Functionalized graphene sheets in dye-sensitized solar cell counter electrodes. Ph.D. Thesis, Princeton University: Princeton, NJ, June 6, 2013.
(3) Hagfeldt, A.; Boschloo, G.; Sun, L.; Kloo, L.; Pettersson, H. *Chem. Rev.* **2010**, *110*, 6595.
(4) Nazeeruddin, M. K.; Zakeeruddin, S. M.; Humphry-Baker, R.; Jirousek, M.; Liska, P.; Vlachopoulos, N.; Shklover, V.; Fischer, C.-H.; Grätzel, M. *Inorg. Chem.* **1999**, *38*, 6298.
(5) Bönnemann, H.; Khelashvili, G.; Behrens, S.; Hinsch, A.; Skupien, K.; Dinjus, E. *J. Cluster Sci.* **2007**, *18*, 141.
(6) Hauch, A.; Georg, A. *Electrochim. Acta* **2001**, *46*, 3457.
(7) Papageorgiou, N.; Maier, W. F.; Gratzel, M. *J. Electrochem. Soc.* **1997**, *144*, 876.
(8) Lee, W. J.; Ramasamy, E.; Lee, D. Y.; Song, J. S. *Sol. Energy Mater. Sol. Cells* **2008**, *92*, 814.
(9) In *Dye-Sensitized Solar Cells*; Kalyanasundaram, K., Ed.; EPFL Press: Lausanne, 2010.
(10) Grätzel, M. *Inorg. Chem.* **2005**, *44*, 6841.
(11) Hardin, B. E.; Snaith, H. J.; McGehee, M. D. *Nat. Photonics* **2012**, *6*, 162.
(12) Mishra, A.; Fischer, M. K. R.; Bäuerle, P. *Angew. Chem., Int. Ed.* **2009**, *48*, 2474.
(13) Li, B.; Wang, L.; Kang, B.; Wang, P.; Qiu, Y. *Sol. Energy Mater. Sol. C* **2006**, *90*, 549.
(14) Chung, I.; Lee, B.; He, J.; Chang, R. P. H.; Kanatzidis, M. G. *Nature* **2012**, *485*, 486.
(15) Yang, L.; Cappel, U. B.; Unger, E. L.; Karlsson, M.; Karlsson, K. M.; Gabrielsson, E.; Sun, L.; Boschloo, G.; Hagfeldt, A.; Johansson, E. M. *Phys. Chem. Chem. Phys.* **2012**, *14*, 779.
(16) Gorlov, M.; Kloo, L. *Dalton Trans.* **2008**, 2655.
(17) Wang, M.; Anghel, A. M.; Marsan, B.; Cevey Ha, N.-L.; Pootrakulchote, N.; Zakeeruddin, S. M.; Grätzel, M. *J. Am. Chem. Soc.* **2009**, *131*, 15976.
(18) Wu, M.; Lin, X.; Wang, Y.; Wang, L.; Guo, W.; Qi, D.; Peng, X.; Hagfeldt, A.; Grätzel, M.; Ma, T. *J. Am. Chem. Soc.* **2012**, *134*, 3419.
(19) Ahmad, S.; Yum, J.-H.; Butt, H.-J.; Nazeeruddin, M. K.; Grätzel, M. *ChemPhysChem* **2010**, *11*, 2814.
(20) Kay, A.; Grätzel, M. *Sol. Energy Mater. Sol. C* **1996**, *44*, 99.
(21) Murakami, T. N.; Ito, S.; Wang, Q.; Nazeeruddin, M. K.; Bessho, T.; Cesar, I.; Liska, P.; Humphry-Baker, R.; Comte, P.; Pechy, P.; Gratzel, M. *J. Electrochem. Soc.* **2006**, *153*, A2255.
(22) Kavan, L.; Yum, J.-H.; Nazeeruddin, M. K.; Grätzel, M. *ACS Nano* **2011**, *5*, 9171.
(23) Roy-Mayhew, J. D.; Boschloo, G.; Hagfeldt, A.; Aksay, I. A. *ACS Appl. Mater. Interfaces* **2012**, *4*, 2794.
(24) Trancik, J. E.; Barton, S. C.; Hone, J. *Nano Lett.* **2008**, *8*, 982.
(25) Suzuki, K.; Yamaguchi, M.; Kumagai, M.; Yanagida, S. *Chem. Lett.* **2003**, *32*, 28.
(26) Wang, X.; Zhi, L.; Mullen, K. *Nano Lett.* **2007**, *8*, 323.
(27) Yan, X.; Cui, X.; Li, B.; Li, L.-s. *Nano Lett.* **2010**, *10*, 1869.
(28) Yang, N.; Zhai, J.; Wang, D.; Chen, Y.; Jiang, L. *ACS Nano* **2010**, *4*, 887.
(29) Chen, T.; Hu, W.; Song, J.; Guai, G. H.; Li, C. M. *Adv. Funct. Mater.* **2012**, *22*, 5245.
(30) Chen, C.; Long, M.; Xia, M.; Zhang, C.; Cai, W. *Nanoscale Res. Lett.* **2012**, *7*, 101.
(31) Ng, Y. H.; Lightcap, I. V.; Goodwin, K.; Matsumura, M.; Kamat, P. V. *J. Phys. Chem. Lett.* **2010**, *1*, 2222.
(32) Peining, Z.; Nair, A. S.; Shengjie, P.; Shengyuan, Y.; Ramakrishna, S. *ACS Appl. Mater. Interfaces* **2012**, *4*, 581.
(33) Wang, H.; Leonard, S. L.; Hu, Y. H. *Ind. Eng. Chem. Res.* **2012**, *51*, 10613.
(34) Durantini, J.; Boix, P. P.; Gervaldo, M.; Morales, G. M.; Otero, L.; Bisquert, J.; Barea, E. M. *J. Electroanal. Chem.* **2012**, *683*, 43.
(35) Jung, M.-H.; Kang, M. G.; Chu, M.-J. *J. Mater. Chem.* **2012**, *22*, 16477.
(36) Ahmad, I.; Khan, U.; Gun'ko, Y. K. *J. Mater. Chem.* **2011**, *21*, 16990.
(37) Roy-Mayhew, J. D.; Bozym, D. J.; Punckt, C.; Aksay, I. A. *ACS Nano* **2010**, *4*, 6203.
(38) Kavan, L.; Yum, J. H.; Grätzel, M. *ACS Nano* **2010**, *5*, 165.
(39) Zhang, D. W.; Li, X. D.; Li, H. B.; Chen, S.; Sun, Z.; Yin, X. J.; Huang, S. M. *Carbon* **2011**, *49*, 5382.
(40) Loh, K. P.; Bao, Q.; Ang, P. K.; Yang, J. *J. Mater. Chem.* **2010**, *20*, 2277.
(41) Park, S.; Ruoff, R. S. *Nat. Nanotechnol.* **2009**, *4*, 217.
(42) Compton, O. C.; Nguyen, S. T. *Small* **2010**, *6*, 711.
(43) Geim, A. K.; Novoselov, K. S. *Nat. Mater.* **2007**, *6*, 183.
(44) Allen, M. J.; Tung, V. C.; Kaner, R. B. *Chem. Rev.* **2010**, *110*, 132.
(45) Huang, X.; Yin, Z.; Wu, S.; Qi, X.; He, Q.; Zhang, Q.; Yan, Q.; Boey, F.; Zhang, H. *Small* **2011**, *7*, 1876.
(46) Mao, S.; Pu, H.; Chen, J. *RSC Adv.* **2012**, *2*, 2643.
(47) Mattevi, C.; Kim, H.; Chhowalla, M. *J. Mater. Chem.* **2010**, *21*, 3324.
(48) Pei, S.; Cheng, H.-M. *Carbon* **2012**, *50*, 3210.
(49) Wintterlin, J.; Bocquet, M. L. *Surf. Sci.* **2009**, *603*, 1841.
(50) Novoselov, K. S.; Falko, V. I.; Colombo, L.; Gellert, P. R.; Schwab, M. G.; Kim, K. *Nature* **2012**, *490*, 192.
(51) Bonaccorso, F.; Sun, Z.; Hasan, T.; Ferrari, A. C. *Nat. Photonics* **2010**, *4*, 611.
(52) Gengler, R. Y.; Spyrou, K.; Rudolf, P. *J. Phys. D: Appl. Phys.* **2010**, *43*, 374015.

(53) Neto, A. C.; Guinea, F.; Peres, N.; Novoselov, K.; Geim, A. *Rev. Mod. Phys.* **2009**, *81*, 109.
(54) Chung, D. *J. Mater. Sci.* **2002**, *37*, 1475.
(55) Novoselov, K.; Geim, A.; Morozov, S.; Jiang, D.; Zhang, Y.; Dubonos, S.; Grigorieva, I.; Firsov, A. *Science* **2004**, *306*, 666.
(56) Novoselov, K.; Jiang, D.; Schedin, F.; Booth, T.; Khotkevich, V.; Morozov, S.; Geim, A. *Proc. Natl. Acad. Sci. U.S.A.* **2005**, *102*, 10451.
(57) Hernandez, Y.; Nicolosi, V.; Lotya, M.; Blighe, F. M.; Sun, Z.; De, S.; McGovern, I. T.; Holland, B.; Byrne, M.; Gun'Ko, Y. K.; Boland, J. J.; Niraj, P.; Duesberg, G.; Krishnamurthy, S.; Goodhue, R.; Hutchison, J.; Scardaci, V.; Ferrari, A. C.; Coleman, J. N. *Nat. Nanotechnol.* **2008**, *3*, 563.
(58) Coleman, J. N. *Acc. Chem. Res.* **2012**, *46*, 14.
(59) Lin, Y.-M.; Dimitrakopoulos, C.; Jenkins, K. A.; Farmer, D. B.; Chiu, H.-Y.; Grill, A.; Avouris, P. *Science* **2010**, *327*, 662.
(60) Berger, C.; Song, Z.; Li, X.; Wu, X.; Brown, N.; Naud, C.; Mayou, D.; Li, T.; Hass, J.; Marchenkov, A. N.; Conrad, E. H.; First, P. N.; de Heer, W. A. *Science* **2006**, *312*, 1191.
(61) Berger, C.; Song, Z.; Li, T.; Li, X.; Ogbazghi, A. Y.; Feng, R.; Dai, Z.; Marchenkov, A. N.; Conrad, E. H.; Phillip, N. *J. Phys. Chem. B* **2004**, *108*, 19912.
(62) Yu, Q.; Jauregui, L. A.; Wu, W.; Colby, R.; Tian, J.; Su, Z.; Cao, H.; Liu, Z.; Pandey, D.; Wei, D. *Nat. Mater.* **2011**, *10*, 443.
(63) Reina, A.; Jia, X.; Ho, J.; Nezich, D.; Son, H.; Bulovic, V.; Dresselhaus, M. S.; Kong, J. *Nano Lett.* **2008**, *9*, 30.
(64) Bolotin, K. I.; Sikes, K.; Jiang, Z.; Klima, M.; Fudenberg, G.; Hone, J.; Kim, P.; Stormer, H. *Solid State Commun.* **2008**, *146*, 351.
(65) Chen, J.-H.; Jang, C.; Xiao, S.; Ishigami, M.; Fuhrer, M. S. *Nat. Nanotechnol.* **2008**, *3*, 206.
(66) Novoselov, K. S.; Geim, A. K.; Morozov, S. V.; Jiang, D.; Katsnelson, M. I.; Grigorieva, I. V.; Dubonos, S. V.; Firsov, A. A. *Nature* **2005**, *438*, 197.
(67) Punckt, C.; Muckel, F.; Wolff, S.; Aksay, I. A.; Chavarin, C. A.; Bacher, G.; Mertin, W. *Appl. Phys. Lett.* **2013**, *102*, 023114.
(68) Lee, C.; Wei, X.; Kysar, J. W.; Hone, J. *Science* **2008**, *321*, 385.
(69) Mak, K. F.; Sfeir, M. Y.; Wu, Y.; Lui, C. H.; Misewich, J. A.; Heinz, T. F. *Phys. Rev. Lett.* **2008**, *101*, 196405.
(70) Peigney, A.; Laurent, C.; Flahaut, E.; Bacsa, R. R.; Rousset, A. *Carbon* **2001**, *39*, 507.
(71) McAllister, M. J.; Li, J.-L.; Adamson, D. H.; Schniepp, H. C.; Abdala, A. A.; Liu, J.; Herrera-Alonso, M.; Milius, D. L.; Car, R.; Prud'homme, R. K.; Aksay, I. A. *Chem. Mater.* **2007**, *19*, 4396.
(72) Brodie, B. C. *Philos. Trans. R. Soc. London* **1859**, *149*, 249.
(73) Staudenmaier, L. *Ber. Dtsch. Chem. Ges.* **1898**, *31*, 1481.
(74) Hofmann, U.; Konig, E. *Z. Anorg. Allg. Chem.* **1937**, *234*, 311.
(75) Hummers, W. S.; Offeman, R. E. *J. Am. Chem. Soc.* **1958**, *80*, 1339.
(76) Marcano, D. C.; Kosynkin, D. V.; Berlin, J. M.; Sinitskii, A.; Sun, Z. Z.; Slesarev, A.; Alemany, L. B.; Lu, W.; Tour, J. M. *ACS Nano* **2010**, *4*, 4806.
(77) Schafhaeutl, C. *J. Prakt. Chem.* **1840**, *21*, 129.
(78) Schniepp, H. C.; Li, J.-L.; McAllister, M. J.; Sai, H.; Herrera-Alonso, M.; Adamson, D. H.; Prud'homme, R. K.; Car, R.; Saville, D. A.; Aksay, I. A. *J. Phys. Chem. B* **2006**, *110*, 8535.
(79) Szabó, T.; Berkesi, O.; Forgó, P.; Josepovits, K.; Sanakis, Y.; Petridis, D.; Dékány, I. *Chem. Mater.* **2006**, *18*, 2740.
(80) Kovtyukhova, N. I.; Ollivier, P. J.; Martin, B. R.; Mallouk, T. E.; Chizhik, S. A.; Buzaneva, E. V.; Gorchinskiy, A. D. *Chem. Mater.* **1999**, *11*, 771.
(81) Yan, J.-A.; Xian, L.; Chou, M. Y. *Phys. Rev. Lett.* **2009**, *103*, 086802.
(82) Hwa, T.; Kokufuta, E.; Tanaka, T. *Phys. Rev. A* **1991**, *44*, R2235.
(83) Wen, X.; Garland, C. W.; Hwa, T.; Kardar, M.; Kokufuta, E.; Li, Y.; Orkisz, M.; Tanaka, T. *Nature* **1992**, *355*, 426.
(84) Dreyer, D. R.; Park, S.; Bielawski, C. W.; Ruoff, R. S. *Chem. Soc. Rev.* **2010**, *39*, 228.
(85) Gao, W.; Alemany, L. B.; Ci, L. J.; Ajayan, P. M. *Nat. Chem.* **2009**, *1*, 403.
(86) Ramesha, G. K.; Sampath, S. *J. Phys. Chem. C* **2009**, *113*, 7985.
(87) Robinson, J. T.; Perkins, F. K.; Snow, E. S.; Wei, Z.; Sheehan, P. E. *Nano Lett.* **2008**, *8*, 3137.
(88) Nemes-Incze, P.; Osváth, Z.; Kamarás, K.; Biró, L. P. *Carbon* **2008**, *46*, 1435.
(89) Lui, C. H.; Li, Z.; Chen, Z.; Klimov, P. V.; Brus, L. E.; Heinz, T. F. *Nano Lett.* **2010**, *11*, 164.
(90) Geng, Y.; Wang, S. J.; Kim, J.-K. *J. Colloid Interface Sci.* **2009**, *336*, 592.
(91) Bajpai, R.; Roy, S.; kulshrestha, N.; Rafiee, J.; Koratkar, N.; Misra, D. S. *Nanoscale* **2012**, *4*, 926.
(92) Prud'Homme, R. K.; Aksay, I. A.; Abdala, A. Thermally Exfoliated Graphite Oxide. U.S. Patent 8,066,964, Nov 29, 2011.
(93) Potts, J. R.; Dreyer, D. R.; Bielawski, C. W.; Ruoff, R. S. *Polymer* **2011**, *52*, 5.
(94) Su, C.-Y.; Xu, Y.; Zhang, W.; Zhao, J.; Liu, A.; Tang, X.; Tsai, C.-H.; Huang, Y.; Li, L.-J. *ACS Nano* **2010**, *4*, 5285.
(95) Zhu, Y.; Murali, S.; Stoller, M. D.; Velamakanni, A.; Piner, R. D.; Ruoff, R. S. *Carbon* **2010**, *48*, 2118.
(96) Chen, W.; Yan, L.; Bangal, P. R. *Carbon* **2010**, *48*, 1146.
(97) Cote, L. J.; Cruz-Silva, R.; Huang, J. *J. Am. Chem. Soc.* **2009**, *131*, 11027.
(98) Matsumoto, Y.; Koinuma, M.; Kim, S. Y.; Watanabe, Y.; Taniguchi, T.; Hatakeyama, K.; Tateishi, H.; Ida, S. *ACS Appl. Mater. Interfaces* **2010**, *2*, 3461.
(99) Nethravathi, C.; Rajamathi, M. *Carbon* **2008**, *46*, 1994.
(100) Wang, H.; Robinson, J. T.; Li, X.; Dai, H. *J. Am. Chem. Soc.* **2009**, *131*, 9910.
(101) Kinoshita, K. *Carbon: Electrochemical and Physicochemical Properties*; John Wiley & Sons: New York, 1987.
(102) Figueiredo, J. L.; Pereira, M. F. R.; Freitas, M. M. A.; Órfão, J. J. M. *Carbon* **1999**, *37*, 1379.
(103) Jung, I.; Field, D. A.; Clark, N. J.; Zhu, Y.; Yang, D.; Piner, R. D.; Stankovich, S.; Dikin, D. A.; Geisler, H.; Ventrice, C. A.; Ruoff, R. S. *J. Phys. Chem. C* **2009**, *113*, 18480.
(104) Lerf, A.; He, H.; Forster, M.; Klinowski, J. *J. Phys. Chem. B* **1998**, *102*, 4477.
(105) Hofmann, U.; Frenzel, A.; Csalán, E. *Justus Liebigs Ann. Chem.* **1934**, *510*, 1.
(106) Bagri, A.; Mattevi, C.; Acik, M.; Chabal, Y. J.; Chhowalla, M.; Shenoy, V. B. *Nat. Chem.* **2010**, *2*, 7.
(107) Campos-Delgado, J.; Kim, Y. A.; Hayashi, T.; Morelos-Gómez, A.; Hofmann, M.; Muramatsu, H.; Endo, M.; Terrones, H.; Shull, R. D.; Dresselhaus, M. S.; Terrones, M. *Chem. Phys. Lett.* **2009**, *469*, 177.
(108) Korkut, S.; Roy-Mayhew, J. D.; Dabbs, D. M.; Milius, D. L.; Aksay, I. A. *ACS Nano* **2011**, *5*, 5214.
(109) Liu, L.-M.; Car, R.; Selloni, A.; Dabbs, D. M.; Aksay, I. A.; Yetter, R. A. *J. Am. Chem. Soc.* **2012**, *134*, 19011.
(110) Pantelides, S. T.; Puzyrev, Y.; Tsetseris, L.; Wang, B. *MRS Bull.* **2012**, *37*, 1187.
(111) Kou, R.; Shao, Y.; Mei, D.; Nie, Z.; Wang, D.; Wang, C.; Viswanathan, V. V.; Park, S.; Aksay, I. A.; Lin, Y. *J. Am. Chem. Soc.* **2011**, *133*, 2541.
(112) Georgakilas, V.; Otyepka, M.; Bourlinos, A. B.; Chandra, V.; Kim, N.; Kemp, K. C.; Hobza, P.; Zboril, R.; Kim, K. S. *Chem. Rev.* **2012**, *112*, 6156.
(113) Chopra, K.; Major, S.; Pandya, D. *Thin Solid Films* **1983**, *102*, 1.
(114) Gordon, R. G. *MRS Bull.* **2000**, *25*, 52.
(115) De, S.; Coleman, J. N. *ACS Nano* **2010**, *4*, 2713.
(116) Zheng, Q.; Ip, W. H.; Lin, X.; Yousefi, N.; Yeung, K. K.; Li, Z.; Kim, J.-K. *ACS Nano* **2011**, *5*, 6039.
(117) Wassei, J. K.; Kaner, R. B. *Mater. Today* **2010**, *13*, 52.
(118) Sukang, B.; Sang Jin, K.; Dolly, S.; Jong-Hyun, A.; Byung Hee, H. *Phys. Scr.* **2012**, *2012*, 014024.
(119) Becerril, H. A.; Mao, J.; Liu, Z.; Stoltenberg, R. M.; Bao, Z.; Chen, Y. *ACS Nano* **2008**, *2*, 463.
(120) Bae, S.; Kim, H.; Lee, Y.; Xu, X.; Park, J.-S.; Zheng, Y.; Balakrishnan, J.; Lei, T.; Ri Kim, H.; Song, Y. I.; Kim, Y.-J.; Kim, K. S.;

Ozyilmaz, B.; Ahn, J.-H.; Hong, B. H.; Iijima, S. *Nat. Nanotechnol.* **2010**, *5*, 574.
(121) Li, C.; Li, Z.; Zhu, H.; Wang, K.; Wei, J.; Li, X.; Sun, P.; Zhang, H.; Wu, D. *J. Phys. Chem. C* **2010**, *114*, 14008.
(122) Tung, V. C.; Chen, L.-M.; Allen, M. J.; Wassei, J. K.; Nelson, K.; Kaner, R. B.; Yang, Y. *Nano Lett.* **2009**, *9*, 1949.
(123) Tien, H. W.; Huang, Y. L.; Yang, S. Y.; Wang, J. Y.; Ma, C. C. M. *Carbon* **2011**, *49*, 1550.
(124) Zhu, Y.; Sun, Z.; Yan, Z.; Jin, Z.; Tour, J. M. *ACS Nano* **2011**, *5*, 6472.
(125) Bi, H.; Sun, S.; Huang, F.; Xie, X.; Jiang, M. *J. Mater. Chem.* **2012**, *22*, 411.
(126) Cottineau, T.; Albrecht, A.; Janowska, I.; Macher, N.; Begin, D.; Ledoux, M. J.; Pronkin, S.; Savinova, E.; Keller, N.; Keller, V.; Pham-Huu, C. *Chem. Commun.* **2012**, *48*, 1224.
(127) Wu, S.; Yin, Z.; He, Q.; Huang, X.; Zhou, X.; Zhang, H. *J. Phys. Chem. C* **2010**, *114*, 11816.
(128) Nazeeruddin, M. K.; Kay, A.; Rodicio, I.; Humphry-Baker, R.; Mueller, E.; Liska, P.; Vlachopoulos, N.; Grätzel, M. *J. Am. Chem. Soc.* **1993**, *115*, 6382.
(129) Koops, S. E.; O'Regan, B. C.; Barnes, P. R. F.; Durrant, J. R. *J. Am. Chem. Soc.* **2009**, *131*, 4808.
(130) Kuang, D.; Ito, S.; Wenger, B.; Klein, C.; Moser, J.-E.; Humphry-Baker, R.; Zakeeruddin, S. M.; Grätzel, M. *J. Am. Chem. Soc.* **2006**, *128*, 4146.
(131) Cameron, P. J.; Peter, L. M. *J. Phys. Chem. B* **2003**, *107*, 14394.
(132) Waita, S. M.; Aduda, B. O.; Mwabora, J. M.; Niklasson, G. A.; Granqvist, C. G.; Boschloo, G. *J. Electroanal. Chem.* **2009**, *637*, 79.
(133) Cameron, P. J.; Peter, L. M.; Hore, S. *J. Phys. Chem. B* **2004**, *109*, 930.
(134) Wang, H.; Peter, L. M. *J. Phys. Chem. C* **2009**, *113*, 18125.
(135) Dunn, H. K.; Peter, L. M. *J. Phys. Chem. C* **2009**, *113*, 4726.
(136) Dunn, H. K.; Westin, P.-O.; Staff, D. R.; Peter, L. M.; Walker, A. B.; Boschloo, G.; Hagfeldt, A. *J. Phys. Chem. C* **2011**, *115*, 13932.
(137) Kim, S. R.; Parvez, M. K.; Chhowalla, M. *Chem. Phys. Lett.* **2009**, *483*, 124.
(138) Tang, B.; Hu, G. *J. Power Sources* **2012**, *220*, 95.
(139) Tang, Y.-B.; Lee, C.-S.; Xu, J.; Liu, Z.-T.; Chen, Z.-H.; He, Z.; Cao, Y.-L.; Yuan, G.; Song, H.; Chen, L.; Luo, L.; Cheng, H.-M.; Zhang, W.-J.; Bello, I.; Lee, S.-T. *ACS Nano* **2010**, *4*, 3482.
(140) Park, J. H.; Seo, S. W.; Kim, J. H.; Choi, C. J.; Kim, H.; Lee, D. K.; Jung, W. S.; Ahn, K. S. *Mol. Cryst. Liq. Cryst.* **2011**, *538*, 285.
(141) Tsai, T. H.; Chiou, S. C.; Chen, S. M. *Int. J. Electrochem. Sci.* **2011**, *6*, 3333.
(142) Zhu, G.; Xu, T.; Lv, T.; Pan, L.; Zhao, Q.; Sun, Z. *J. Electroanal. Chem.* **2011**, *650*, 248.
(143) He, Z.; Guai, G.; Liu, J.; Guo, C.; Loo, J. S. C.; Li, C. M.; Tan, T. T. Y. *Nanoscale* **2011**, *3*, 4613.
(144) Sun, S.; Gao, L.; Liu, Y. *Appl. Phys. Lett.* **2010**, *96*, 083113.
(145) Bell, N. J.; Ng, Y. H.; Du, A.; Coster, H.; Smith, S. C.; Amal, R. *J. Phys. Chem. C* **2011**, *115*, 6004.
(146) Hu, X.; Huang, K.; Fang, D.; Liu, S. *Mater. Sci. Eng., B* **2011**, *176*, 431.
(147) Fang, X.; Li, M.; Guo, K.; Zhu, Y.; Hu, Z.; Liu, X.; Chen, B.; Zhao, X. *Electrochim. Acta* **2012**, *65*, 174.
(148) Peter, L. *Acc. Chem. Res.* **2009**, *42*, 1839.
(149) Chappel, S.; Chen, S.-G.; Zaban, A. *Langmuir* **2002**, *18*, 3336.
(150) Chappel, S.; Grinis, L.; Ofir, A.; Zaban, A. *J. Phys. Chem. B* **2005**, *109*, 1643.
(151) Joanni, E.; Savu, R.; de Sousa Góes, M.; Bueno, P. R.; de Freitas, J. N.; Nogueira, A. F.; Longo, E.; Varela, J. A. *Scr. Mater.* **2007**, *57*, 277.
(152) Ramanathan, T.; Abdala, A. A.; Stankovich, S.; Dikin, D. A.; Herrera-Alonso, M.; Piner, R. D.; Adamson, D. H.; Schniepp, H. C.; Chen, X.; Ruoff, R. S.; Nguyen, S. T.; Aksay, I. A.; Prud'Homme, R. K.; Brinson, L. C. *Nat. Nanotechnol.* **2008**, *3*, 327.
(153) Song, J.; Yin, Z.; Yang, Z.; Amaladass, P.; Wu, S.; Ye, J.; Zhao, Y.; Deng, W.-Q.; Zhang, H.; Liu, X.-W. *Chem.—Eur. J.* **2011**, *17*, 10832.
(154) Zhang, H.; Lv, X.; Li, Y.; Wang, Y.; Li, J. *ACS Nano* **2009**, *4*, 380.
(155) Zhang, Y.; Tang, Z.-R.; Fu, X.; Xu, Y.-J. *ACS Nano* **2011**, *5*, 7426.
(156) Kim, A. Y.; Kim, J.; Kim, M. Y.; Ha, S. W.; Ngyen, T. T. T.; Kang, M. *Bull. Korean Chem. Soc.* **2012**, *33*, 3355.
(157) Hoshikawa, T.; Yamada, M.; Kikuchi, R.; Eguchi, K. *J. Electrochem. Soc.* **2005**, *152*, E68.
(158) Fabregat-Santiago, F.; Bisquert, J.; Garcia-Belmonte, G.; Boschloo, G.; Hagfeldt, A. *Sol. Energy Mater. Sol. C* **2005**, *87*, 117.
(159) Wang, Q.; Moser, J.-E.; Grätzel, M. *J. Phys. Chem. B* **2005**, *109*, 14945.
(160) Fabregat-Santiago, F.; Garcia-Belmonte, G.; Mora-Sero, I.; Bisquert, J. *Phys. Chem. Chem. Phys.* **2011**, *13*, 9083.
(161) Kern, R.; Sastrawan, R.; Ferber, J.; Stangl, R.; Luther, J. *Electrochim. Acta* **2002**, *47*, 4213.
(162) Fabregat-Santiago, F.; Bisquert, J.; Palomares, E.; Otero, L.; Kuang, D.; Zakeeruddin, S. M.; Grätzel, M. *J. Phys. Chem. C* **2007**, *111*, 6550.
(163) Adachi, M.; Sakamoto, M.; Jiu, J.; Ogata, Y.; Isoda, S. *J. Phys. Chem. B* **2006**, *110*, 13872.
(164) Greijer Agrell, H.; Boschloo, G.; Hagfeldt, A. *J. Phys. Chem. B* **2004**, *108*, 12388.
(165) Diebold, U. *Surf. Sci. Rep.* **2003**, *48*, 53.
(166) Fan, J.; Liu, S.; Yu, J. *J. Mater. Chem.* **2012**, *22*, 17027.
(167) Li, Y.; Wang, G.; Pan, K.; Jiang, B.; Tian, C.; Zhou, W.; Fu, H. *J. Mater. Chem.* **2012**, *22*, 20381.
(168) Yang, H.; Guo, C.; Guai, G. H.; Song, Q.; Jiang, S. P.; Li, C. M. *ACS Appl. Mater. Interfaces* **2011**, *3*, 1940.
(169) Yang, H.; Guai, G. H.; Guo, C.; Song, Q.; Jiang, S. P.; Wang, Y.; Zhang, W.; Li, C. M. *J. Phys. Chem. C* **2011**, *115*, 12209.
(170) Neo, C. Y.; Ouyang, J. *J. Power Sources* **2013**, *222*, 161.
(171) Williams, K. J.; Nelson, C. A.; Yan, X.; Li, L.-S.; Zhu, X. *ACS Nano* **2013**, *4*, 1388.
(172) Tielrooij, K. J.; Song, J. C. W.; Jensen, S. A.; Centeno, A.; Pesquera, A.; Zurutuza Elorza, A.; Bonn, M.; Levitov, L. S.; Koppens, F. H. L. *Nat. Phys.* **2013**, *9*, 248.
(173) Long, R.; English, N. J.; Prezhdo, O. V. *J. Am. Chem. Soc.* **2012**, *134*, 14238.
(174) Zhang, Y.; Zhang, N.; Tang, Z.-R.; Xu, Y.-J. *ACS Nano* **2012**, *6*, 9777.
(175) Yan, X.; Li, B.; Cui, X.; Wei, Q.; Tajima, K.; Li, L.-s. *J. Phys. Chem. Lett.* **2011**, *2*, 1119.
(176) Hamilton, I. P.; Li, B.; Yan, X.; Li, L.-S. *Nano Lett.* **2011**, *11*, 1524.
(177) Peng, J.; Gao, W.; Gupta, B. K.; Liu, Z.; Romero-Aburto, R.; Ge, L.; Song, L.; Alemany, L. B.; Zhan, X.; Gao, G.; Vithayathil, S. A.; Kaipparettu, B. A.; Marti, A. A.; Hayashi, T.; Zhu, J.-J.; Ajayan, P. M. *Nano Lett.* **2012**, *12*, 844.
(178) Mohanty, N.; Moore, D.; Xu, Z.; Sreeprasad, T. S.; Nagaraja, A.; Rodriguez, A. A.; Berry, V. *Nat. Commun.* **2012**, *3*, 844.
(179) Lin, L.; Zhang, S. *Chem. Commun.* **2012**, *48*, 10177.
(180) Velten, J. A.; Carretero-González, J.; Castillo-Martínez, E.; Bykova, J.; Cook, A.; Baughman, R.; Zakhidov, A. *J. Phys. Chem. C* **2011**, *115*, 25125.
(181) Hamann, T. W. *Dalton Trans.* **2012**, *41*, 3111.
(182) Gun, J.; Kulkarni, S. A.; Xiu, W.; Batabyal, S. K.; Sladkevich, S.; Prikhodchenko, P. V.; Gutkin, V.; Lev, O. *Electrochem. Commun.* **2012**, *19*, 108.
(183) Neo, C. Y.; Ouyang, J. *Carbon* **2013**, *54*, 48.
(184) Bai, H.; Li, C.; Wang, X.; Shi, G. *J. Phys. Chem. C* **2011**, *115*, 5545.
(185) Pope, M. A.; Korkut, S.; Punckt, C.; Aksay, I. A. *J. Electrochem. Soc.* **2013**, *160*, A1653.
(186) Murakami, T. N.; Gratzel, M. *Inorg. Chim. Acta* **2008**, *361*, 572.
(187) Olsen, E.; Hagen, G.; Lindquist, E. S. *Sol. Energy Mater. Sol. C* **2000**, *63*, 267.

(188) Desilvestro, H.; Boz, M.; Tulloch, S.; Tulloch, G. In *Dye-Sensitized Solar Cells*; Kalyanasundaram, K., Ed.; EPFL Press: Lausanne, 2010.
(189) Hong, W.; Xu, Y.; Lu, G.; Li, C.; Shi, G. *Electrochem. Commun.* **2008**, *10*, 1555.
(190) Bard, A. J.; Faulkner, L. R. *Electrochemical Methods: Fundamentals and Applications*, 2nd ed.; John Wiley & Sons: New York, 2001.
(191) Fang, X.; Ma, T.; Guan, G.; Akiyama, M.; Kida, T.; Abe, E. *J. Electroanal. Chem.* **2004**, *570*, 257.
(192) Kim, J.-M.; Rhee, S.-W. *Electrochim. Acta* **2012**, *83*, 264.
(193) Kwon, W.; Kim, J.-M.; Rhee, S.-W. *Electrochim. Acta* **2012**, *68*, 110.
(194) Dou, Y.; Li, G.; Song, J.; Gao, X. *Phys. Chem. Chem. Phys.* **2012**, *14*, 1339.
(195) Li, G. R.; Song, J.; Pan, G. L.; Gao, X. P. *Energy Environ. Sci.* **2011**, *4*, 1680.
(196) Menshykau, D.; Compton, R. G. *Electroanalysis* **2008**, *20*, 2387.
(197) Punckt, C.; Pope, M. A.; Liu, J.; Lin, Y.; Aksay, I. A. *Electroanaysis* **2010**, *22*, 2834.
(198) Xu, Y.; Bai, H.; Lu, G.; Li, C.; Shi, G. *J. Am. Chem. Soc.* **2008**, *130*, 5856.
(199) Choi, S. H.; Ju, H. M.; Huh, S. H.; Song, C. K.; Park, S. H.; Kim, B. M. *J. Korean Phys. Soc.* **2010**, *57*, 1653.
(200) Hasin, P.; Alpuche-Aviles, M. A.; Wu, Y. *J. Phys. Chem. C* **2010**, *114*, 15857.
(201) Choi, H.; Kim, H.; Hwang, S.; Han, Y.; Jeon, M. *J. Mater. Chem.* **2011**, *21*, 7548.
(202) Hsieh, C.-T.; Yang, B.-H.; Chen, Y.-F. *Diamond Relat. Mater.* **2012**, *27*−*28*, 68.
(203) Jang, S.-Y.; Kim, Y.-G.; Kim, D. Y.; Kim, H.-G.; Jo, S. M. *ACS Appl. Mater. Interfaces* **2012**, *4*, 3500.
(204) Jang, H.-S.; Yun, J.-M.; Kim, D.-Y.; Park, D.-W.; Na, S.-I.; Kim, S.-S. *Electrochim. Acta* **2012**, *81*, 301.
(205) Wan, L.; Wang, S.; Wang, X.; Dong, B.; Xu, Z.; Zhang, X.; Yang, B.; Peng, S.; Wang, J.; Xu, C. *Solid State Sci.* **2011**, *13*, 468.
(206) Wu, M.-S.; Zheng, Y.-J. *Phys. Chem. Chem. Phys.* **2013**, *15*, 1782.
(207) Zheng, H.; Neo, C. Y.; Mei, X.; Qiu, J.; Ouyang, J. *J. Mater. Chem.* **2012**, *22*, 14465.
(208) Lee, J.-S.; Ahn, H.-J.; Yoon, J.-C.; Jang, J.-H. *Phys. Chem. Chem. Phys.* **2012**, *14*, 7938.
(209) Gong, F.; Li, Z.; Wang, H.; Wang, Z.-S. *J. Mater. Chem.* **2012**, *22*, 17321.
(210) Yen, M.-Y.; Hsieh, C.-K.; Teng, C.-C.; Hsiao, M.-C.; Liu, P.-I.; Ma, C.-C. M.; Tsai, M.-C.; Tsai, C.-H.; Lin, Y.-R.; Chou, T.-Y. *RSC Adv.* **2012**, *2*, 2725.
(211) Xue, Y.; Liu, J.; Chen, H.; Wang, R.; Li, D.; Qu, J.; Dai, L. *Angew. Chem., Int. Ed.* **2012**, *51*, 12124.
(212) Das, S.; Sudhagar, P.; Verma, V.; Song, D.; Ito, E.; Lee, S. Y.; Kang, Y. S.; Choi, W. *Adv. Funct. Mater.* **2011**, *21*, 3729.
(213) Das, S.; Sudhagar, P.; Ito, E.; Lee, D.-y.; Nagarajan, S.; Lee, S. Y.; Kang, Y. S.; Choi, W. *J. Mater. Chem.* **2012**, *22*, 20490.
(214) Li, S.; Luo, Y.; Lv, W.; Yu, W.; Wu, S.; Hou, P.; Yang, Q.; Meng, Q.; Liu, C.; Cheng, H.-M. *Adv. Energy Mater.* **2011**, *1*, 486.
(215) Bajpai, R.; Roy, S.; Kumar, P.; Bajpai, P.; Kulshrestha, N.; Rafiee, J.; Koratkar, N.; Misra, D. S. *ACS Appl. Mater. Interfaces* **2011**, *3*, 3884.
(216) Kavan, L.; Yum, J.-H.; Grätzel, M. *Nano Lett.* **2011**, *11*, 5501.
(217) Velten, J.; Mozer, A. J.; Li, D.; Officer, D.; Wallace, G.; Baughman, R.; Zakhidov, A. *Nanotechnology* **2012**, *23*, 085201.
(218) Zhu, G.; Pan, L.; Lu, T.; Xu, T.; Sun, Z. *J. Mater. Chem.* **2011**, *21*, 14869.
(219) Chang, L.-H.; Hsieh, C.-K.; Hsiao, M.-C.; Chiang, J.-C.; Liu, P.-I.; Ho, K.-K.; Ma, C.-C. M.; Yen, M.-Y.; Tsai, M.-C.; Tsai, C.-H. *J. Power Sources* **2013**, *222*, 518.
(220) Kim, H.; Choi, H.; Hwang, S.; Kim, Y.; Jeon, M. *Nanoscale Res. Lett.* **2012**, *7*, 53.
(221) Kaniyoor, A.; Ramaprabhu, S. *J. Appl. Phys.* **2011**, *109*, 124308.
(222) Li, Z.-Y.; Shaheer Akhtar, M.; Hee Kuk, J.; Kong, B.-S.; Yang, O. B. *Mater. Lett.* **2012**, *86*, 96.
(223) Lee, K. S.; Lee, Y.; Lee, J. Y.; Ahn, J.-H.; Park, J. H. *ChemSusChem* **2012**, *5*, 379.
(224) Wang, G.; Xing, W.; Zhuo, S. *Electrochim. Acta* **2012**, *66*, 151.
(225) Gong, F.; Xu, X.; Zhou, G.; Wang, Z.-S. *Phys. Chem. Chem. Phys.* **2013**, *15*, 546.
(226) Kaniyoor, A.; Ramaprabhu, S. *J. Mater. Chem.* **2012**, *22*, 8377.
(227) Gong, F.; Wang, H.; Wang, Z. S. *Phys. Chem. Chem. Phys.* **2011**, *13*, 17676.
(228) Tjoa, V.; Chua, J.; Pramana, S. S.; Wei, J.; Mhaisalkar, S. G.; Mathews, N. *ACS Appl. Mater. Interfaces* **2012**, *4*, 3447.
(229) Li, P.-J.; Chen, K.; Chen, Y.-F.; Wang, Z.-G.; Hao, X.; Liu, J.-B.; He, J.-R.; Zhang, W.-L. *Chin. Phys. B* **2012**, *21*, 118101.
(230) Chartarrayawadee, W.; Moulton, S. E.; Li, D.; Too, C. O.; Wallace, G. G. *Electrochim. Acta* **2012**, *60*, 213.
(231) Yen, M.-Y.; Teng, C.-C.; Hsiao, M.-C.; Liu, P.-I.; Chuang, W.-P.; Ma, C.-C. M.; Hsieh, C.-K.; Tsai, M.-C.; Tsai, C.-H. *J. Mater. Chem.* **2011**, *21*, 12880.
(232) Das, S.; Sudhagar, P.; Nagarajan, S.; Ito, E.; Lee, S. Y.; Kang, Y. S.; Choi, W. *Carbon* **2012**, *50*, 4815.
(233) Radich, J. G.; Dwyer, R.; Kamat, P. V. *J. Phys. Chem. Lett.* **2011**, *2*, 2453.
(234) Lin, J.-Y.; Chan, C.-Y.; Chou, S.-W. *Chem. Commun.* **2013**, *49*, 1440.
(235) Liu, C.-J.; Tai, S.-Y.; Chou, S.-W.; Yu, Y.-C.; Chang, K.-D.; Wang, S.; Chien, F. S.-S.; Lin, J.-Y.; Lin, T.-W. *J. Mater. Chem.* **2012**, *22*, 21057.
(236) Santra, P. K.; Kamat, P. V. *J. Am. Chem. Soc.* **2012**, *134*, 2508.
(237) Meier, D. L.; Chandrasekaran, V.; Gupta, A.; Yelundur, V.; Rohatgi, A. *IEEE J. Photovol.* **2013**, *3*, 199.
(238) Liu, Z.; Liu, Q.; Huang, Y.; Ma, Y.; Yin, S.; Zhang, X.; Sun, W.; Chen, Y. *Adv. Mater.* **2008**, *20*, 3924.
(239) Hu, Y. H.; Wang, H.; Hu, B. *ChemSusChem* **2010**, *3*, 782.
(240) Guo, C. X.; Guai, G. H.; Li, C. M. *Adv. Energy Mater.* **2011**, *1*, 448.
(241) Sun, Y.; Wu, Q.; Shi, G. *Energy Environ. Sci.* **2011**, *4*, 1113.
(242) Zhang, L.; Fan, L.; Li, Z.; Shi, E.; Li, X.; Li, H.; Ji, C.; Jia, Y.; Wei, J.; Wang, K.; Zhu, H.; Wu, D.; Cao, A. *Nano Res.* **2011**, *4*, 891.
(243) Li, X.; Zhu, H.; Wang, K.; Cao, A.; Wei, J.; Li, C.; Jia, Y.; Li, Z.; Li, X.; Wu, D. *Adv. Mater.* **2010**, *22*, 2743.
(244) Miao, X.; Tongay, S.; Petterson, M. K.; Berke, K.; Rinzler, A. G.; Appleton, B. R.; Hebard, A. F. *Nano Lett.* **2012**, *12*, 2745.
(245) Liang, Y.; Li, Y.; Wang, H.; Zhou, J.; Wang, J.; Regier, T.; Dai, H. *Nat. Mater.* **2011**, *10*, 780.
(246) Kamat, P. V. *J. Phys. Chem. Lett.* **2011**, *2*, 242.
(247) Cui, S.; Mao, S.; Lu, G.; Chen, J. *J. Phys. Chem. Lett.* **2013**, *4*, 2441.
(248) Gabor, N. M.; Song, J. C. W.; Ma, Q.; Nair, N. L.; Taychatanapat, T.; Watanabe, K.; Taniguchi, T.; Levitov, L. S.; Jarillo-Herrero, P. *Science* **2011**, *334*, 648.
(249) Song, J. C. W.; Rudner, M. S.; Marcus, C. M.; Levitov, L. S. *Nano Lett.* **2011**, *11*, 4688.